Developments in the Built Environment 26 (2026) 100919



Contents lists available at ScienceDirect

Developments in the Built Environment

journal homepage: www.sciencedirect.com/journal/developments-in-the-built-environment



Machine-learning-based prediction of the compressive strength of superabsorbent polymer-incorporated cementitious materials: Modeling and experimental insights into polymer characteristics

Dohyeong Kim [a,1], Sangwoo Oh [b,1], Seongcheol Choi [b], Geuntae Hong [a,*]

[a] Department of Civil Engineering, Kyungpook National University, 80 Daehak-ro, Buk-gu, Daegu, 41566, Republic of Korea
[b] Department of Civil and Environmental Engineering, Chung-Ang University, 84 Heukseok-ro, Dongjak-gu, Seoul, 06974, Republic of Korea

ARTICLE INFO

Keywords:
Compressive strength
Machine learning
Superabsorbent polymer
X-ray micro-computed tomography

ABSTRACT

To predict the compressive strength of superabsorbent polymer (SAP)-incorporated cementitious materials, this study developed machine-learning-based models incorporating SAP characteristics (particle size, shape, type, and absorption capacity) and evaluated them in tandem with using X-ray micro-computed tomography (CT) and compressive strength testing of the resulting cementitious material. CatBoost provided the best performance (coefficient of determination = 0.9680 and accuracy = 92.70%) owing to its effective handling of nonlinearity and feature interactions, as well as its robust treatment of categorical variables through ordered boosting and target statistics. The relative importance of the SAP-related input features affecting compressive strength prediction followed the order of absorption capacity, dosage amount, type, particle size, and shape. Experimental observations combining X-ray micro-CT measurements and compressive strength testing confirm that in addition to total porosity, variations in pore distribution, shape, and hydration degree induced by SAPs contributed to the compressive strength of the cementitious material.

1. Introduction

Concrete is the most widely used construction material worldwide owing to its low material cost, easy and local availability of raw ingredients, and flexible mix design that can be tailored to achieve the target performance requirements such as strength, workability, and durability (Adesina and Zhang, 2024). Among the various mechanical properties, compressive strength is a key performance indicator that directly reflects the load-bearing capacity of structural members under axial and flexural loads (Singh et al., 2022). This makes it a fundamental criterion for assessing the safety and durability of infrastructures such as buildings, bridges, and pavements, so accurate prediction thereof is essential to ensure structural reliability, compliance with design specifications, and quality control (Kumar et al., 2024).

In this context, the compressive strength of cementitious materials is mostly determined through standardized experimental testing. In addition, several empirical regression models have been proposed using concrete mix constituents and proportions based on accumulated experimental data as input variables to predict the compressive strength of cementitious materials. Numerical approaches simulating material and structural behavior have also been employed for compressive strength prediction (Feng et al., 2020). However, conventional strength testing requires a curing period of 28 days and entails the cost of specimen preparation and testing (Nithurshan and Elakneswaran, 2023). Furthermore, empirical models often exhibit limited generalizability when applied beyond their calibration domain and lack flexibility to accommodate newly introduced input variables (Chaabene et al., 2020). In particular, variations in raw materials and mix proportions influence hydration reactions, pore structure, and the quality of the interfacial transition zone between the cement paste and the aggregates, thereby altering the load-bearing matrix of the cementitious material. Because these criteria affect the compressive strength of the material in a nonlinear and interactive manner (Pressmair et al., 2022), fully capturing the complex physicochemical behavior of cementitious materials is difficult using traditional approaches and limits their predictive reliability.

With the diversification of raw materials and the increasing complexity of mix proportions to impart new functionalities to

* Corresponding author.
E-mail address: gthong@knu.ac.kr (G. Hong).
[1] These authors contributed equally to this work and should be considered co-first authors.

https://doi.org/10.1016/j.dibe.2026.100919
Received 6 January 2026; Received in revised form 28 February 2026; Accepted 2 April 2026
Available online 3 April 2026
2666-1659/© 2026 The Authors. Published by Elsevier Ltd. This is an open access article under the CC BY-NC-ND license (http://creativecommons.org/licenses/by-nc-nd/4.0/).

cementitious materials, the difficulty of predicting the properties of the latter has continued to grow, a trend that has been particularly intensified by the introduction of novel admixtures (Ni et al., 2025). Among them, superabsorbent polymers (SAPs) have attracted increasing research attention owing to their ability to absorb and release water, which facilitates internal curing and self-healing, thereby mitigating shrinkage and enhancing durability (Schröfl et al., 2022). However, incorporating SAPs can lead to the formation of numerous pores, which can deteriorate the mechanical performance of the resulting cementitious material (Chen et al., 2025), while also influencing other properties such as freeze–thaw resistance and permeability. The magnitude and direction of these effects reportedly depend on the intrinsic characteristics of the SAP, including particle size, dosage amount, particle morphology, and type (Lyu et al., 2021). Consequently, despite their functional benefits, the complex property variations induced by introducing a SAP constrain the accurate prediction, control, and performance-based mix design of the resulting cementitious material.

Recently, machine-learning (ML) techniques have been increasingly adopted as an alternative approach to overcome the limitations of conventional compressive strength prediction methods (Nguyen et al., 2021). Al-Jamimi et al. (2022) developed a hybrid model combining a support vector machine (SVM) with a genetic algorithm (GA) to predict the compressive strength of plain and blended cement-based concretes; in the testing phase, the model achieved a coefficient of determination (R^2) > 0.992 and outperformed conventional regression-based models. Asadi Shamsabadi et al. (2022) modeled the compressive strength of concrete incorporating waste marble powder (WMP) using various ML techniques; their analysis revealed that extreme gradient boosting (XGB) and artificial neural network (ANN) models exhibited high predictive accuracy ($R^2 > 0.97$), with the ANN model showing higher sensitivity to variations in WMP content. Seki et al. (2024) applied ML models to predict the compressive strength of alkali-activated materials (AAMs) by considering the composition ratio of blast furnace slag (BFS) and fly ash (FA). They reported that the influence of FA composition on compressive strength was greater than that of BFS and that model performance improved when the dataset was classified into FA-based and BFS-based AAMs. Collectively, these studies demonstrate the potential of ML in learning and representing the complex nonlinear interactions among diverse mix variables, thereby enabling the comprehensive prediction of property changes associated with the introduction of admixtures. From this perspective, ML offers a promising alternative for predicting the properties of cementitious materials incorporating SAPs.

Accordingly, recent studies have increasingly employed ML techniques to predict the properties of cementitious materials with incorporated SAPs (Hilloulin and Tran, 2022; Qureshi et al., 2022; Barkhordari et al., 2024; Hosseinzadeh et al., 2024). In these studies, ML has been used to predict autogenous shrinkage and strength-related outcomes using datasets compiled from published experimental results. The input features commonly include mixture proportions together with SAP-related variables such as SAP dosage, particle size, and water uptake. However, most of these studies have primarily focused on mitigating autogenous shrinkage, while comprehensive modeling that simultaneously considers the intrinsic characteristics of SAPs (particle size, shape, type, and absorption capacity) remains limited. As a result, compressive strength prediction does not readily generalize across SAP systems, because the input variables used in prior ML studies often do not capture intrinsic SAP characteristics in a consistent and comprehensive manner. This is important since SAP affects moisture redistribution and pore formation in the hardened matrix, and these microstructural changes govern compressive strength. Therefore, it is necessary to clarify the role of multi-dimensional SAP characteristics in compressive strength prediction and to support such data-driven findings with microstructural evidence for more reliable prediction and clearer interpretation.

To address these challenges, this study developed ML-based models to predict the compressive strength of SAP-incorporated cementitious materials, in which the intrinsic characteristics of the SAPs (particle size, shape, type, and absorption capacity) were explicitly incorporated as input variables. Five representative ML techniques, namely ANN, SVM, and three decision tree (DT)-based techniques (random forest (RF), XGBoost, and CatBoost), were implemented and quantitatively compared in terms of predictive performance, while feature importance analysis was conducted to identify the factors that significantly contribute to compressive strength. Furthermore, the model interpretation results were complementarily examined in conjunction with experimental data, including compressive strength measurements and pore structure indicators obtained from X-ray micro-computed tomography (CT), to elucidate the influence of SAP characteristics on compressive strength. Finally, the GA was employed to calibrate and extend the conventional porosity–strength relationship by parameterizing additional variables associated with SAP characteristics. The following are the specific objectives that hold research significance:

i. To demonstrate that explicitly representing intrinsic SAP characteristics is critical for reliable compressive strength prediction across SAP systems
ii. To interpret the learned relationships by connecting explainable ML trends with microstructural evidence from X-ray micro-CT
iii. To provide practical insight by translating multi-dimensional SAP characteristics into a simplified descriptor for strength-oriented mix design

2. Theoretical background

2.1. Overview of ML

ML, a subfield of artificial intelligence, is a data-driven computational approach that enables computers to learn patterns and relationships from data and construct predictive models without the need for explicitly programmed rules. Such models extract latent patterns from empirical datasets and generalize them, thereby enabling them to perform predictive tasks such as classification and regression. With advances in algorithms, computational power, and the availability of large-scale datasets, ML has rapidly expanded over the past decades and is now extensively applied across various scientific and engineering domains (Tran, 2022). In the present study, five ML techniques that are widely adopted in the field of construction materials (ANN, SVM, and three DT-based techniques) were employed to develop predictive models for incorporating SAPs into cementitious materials, and their performances were compared.

2.2. ML techniques

2.2.1. ANN

This is a hierarchical technique inspired by the functioning of the biological nervous system and consists of interconnected artificial neurons (nodes) (Maier et al., 2023). It is composed of an input layer, one or more hidden layers, and an output layer, where the interconnections between neurons are governed by weights and biases (Prasad et al., 2009). The operation of a hidden neuron can be expressed as follows:

$$y = f\left(\sum_{i=1}^{n}(w_i x_i) + b\right), \tag{1}$$

where y is the output of the neuron, f is the activation function that introduces nonlinearity into the network, b is the bias term, and w_i and x_i are the weights and input values, respectively (Li et al., 2024). When multiple hidden layers are stacked, the network is referred to as a Deep Neural Network (DNN), which enables the progressive learning of hierarchical representations from the input data (Lauriola et al., 2020). This architecture allows the network to learn high-level features compared to shallow networks and to better approximate complex

nonlinear functions (Li et al., 2023).

The activation function determines the representational capacity and learning stability of neural networks and plays a critical role throughout the computational process, including forward and backward propagation (Zhang and Ding, 2025). In early neural networks, the sigmoid and tanh functions were commonly used as activation functions. However, the gradients approach zero in their saturated regions, leading to the vanishing gradient problem, which limits the training capability of deep networks. As an alternative, the rectified linear unit (ReLU) (defined in Eq. (2)) has been widely adopted and is now considered the de facto standard activation function in deep-learning architectures (Kiliçarslan and Celik, 2021). Nevertheless, ReLU sets negative inputs to zero, which can cause some neurons to remain inactive for long periods, a phenomenon known as "the dying ReLU problem" (Liang and Xu, 2021). To address this limitation, the Gaussian error linear unit (GeLU) (defined in Eq. (3)) introduces a probabilistic gating mechanism by multiplying each input by the cumulative distribution function of the standard normal distribution. This provides smoother nonlinearity, which avoids the abrupt cutoff of ReLU and results in more stable gradient propagation during training. Considering these advantages, this study constructed an ANN-based DNN architecture employing the GeLU activation function.

$$\mathrm{ReLU}(x) = \max(x, 0), x \in \mathbb{R}, \tag{2}$$

$$\mathrm{GeLU}(x) = x \cdot \Phi(x) = 0.5x\left(\tanh\left[\frac{\sqrt{2}}{\pi}\left(x + 0.044715x^3\right)\right]\right), \tag{3}$$

where $\Phi(x)$ denotes the cumulative distribution function of the standard normal distribution (Aby et al., 2025).

2.2.2. SVM

A supervised learning technique for classification and regression, SVM is known for its strong generalization performance even in high-dimensional feature spaces (Wang et al., 2016). It is particularly effective in high-dimensional, small sample size settings where the number of features exceeds the number of observations (Nakayama et al., 2017). SVM determines the optimal decision boundary by identifying the hyperplane that maximizes the margin, which is defined as the minimum distance between the hyperplane and the nearest data points from each class (Chen et al., 2010). Consequently, the resulting model depends primarily on the support vectors (the training samples lying closest to the separating hyperplane) rather than on the entire training data distribution (Cervantes et al., 2020). A detailed mathematical derivation for the optimal separating hyperplane can be found in (Cortes and Vapnik, 1995).

For problems that are not linearly separable, the kernel trick is employed to map the original nonlinear data into a higher-dimensional feature space, where the transformed data become linearly separable (Hussain, 2019). Kernel Ridge Regression (KRR) is a regression technique based on the kernel trick, in which nonlinear relationships are modeled by replacing explicit feature mappings with kernel functions that implicitly compute inner products in a high-dimensional feature space (Douak et al., 2013). It is particularly useful for regression tasks involving complex nonlinear relationships. By leveraging kernel functions to project data into a higher-dimensional feature space, KRR can capture intricate patterns and achieve more accurate predictions (Ran et al., 2024).

2.2.3. DT – bagging

RF algorithms are a combination of tree predictors and can yield significant improvements in classification accuracy, while overfitting is not a problem as the number of trees increases (Breiman, 2001). During training, it produces multiple DTs using randomly selected subsets of training samples and variables (Belgiu and Drăguţ, 2016). For regression, the prediction is obtained by averaging the outputs of many trees fitted to bootstrap-sampled versions of the training data (Hastie et al., 2009). The prediction of a RF regression model consisting of K trees can be expressed as follows:

$$\hat{y} = \frac{1}{K}\sum_{k=1}^{K} h_k(x), \tag{4}$$

where $\hat{y}$ is the final predicted value, K is the total number of trees in the forest, and $h_k(x)$ represents the output of the k-th DT for the input vector x (Breiman, 2001).

RF uses bootstrap aggregating, meaning that an ensemble is formed by applying the base learner to bootstrap samples of the learning sample (Sexton and Laake, 2009). In addition, RF selects a random subset of explanatory variables when choosing a splitting variable in a tree, which reduces correlation among trees and thereby reduces variance and improves prediction accuracy compared with a single tree or ordinary bagging trees (Song, 2015). RF provides an internal performance estimate based on out-of-bag samples produced by the standard training process, which enables an efficient assessment of accuracy or generalization error without explicit data splitting (Cánovas-García et al., 2017; C and Marques, 2022). RF provides variable importance measures, and its popular and widely used permutation-based variable importance has motivated ongoing research on statistical inference and hypothesis testing for variable importance (Hapfelmeier et al., 2023).

2.2.4. DT – XGBoost

XGBoost belongs to the boosting family in which base learners are generated sequentially and combined to form a stronger predictor (Freund and Schapire, 1997). From a statistical learning perspective, gradient boosting constructs an additive model via stage-wise functional optimization, where each stage follows a gradient-descent direction defined by the chosen loss (Friedman, 2001). When DTs are used as base learners, boosting can be interpreted as iteratively fitting an additive rule by successively updating the model using information from the current fit, which provides a principled view of why sequential ensembles can outperform a single tree (Friedman et al., 2000). To improve robustness and reduce overfitting, stochastic gradient boosting introduces randomness by drawing a subsample of the training data at each iteration, which can improve both accuracy and computational efficiency in practice (Friedman, 2002). In XGBoost, the prediction is written as an additive sum of K tree functions and the training objective explicitly includes a regularization term that penalizes model complexity, which is a key design choice for controlling overfitting while preserving high predictive performance:

$$\hat{y}_i = \phi(x_i) = \sum_{k=1}^{K} f_k(x_i), f_k \in \mathscr{F}, \tag{5}$$

where x_i is the input vector, $\hat{y}_i$ is the prediction, K is the number of trees, and f_k denotes the k-th regression tree in the function space $\mathscr{F}$ (Chen et al., 2016).

$$\mathscr{L}(\phi) = \sum_i l(y_i, \hat{y}_i) + \sum_k \Omega(f_k), \tag{6}$$

where y_i is the target value, $l(\cdot)$ is the loss function, and $\Omega(\cdot)$ is the regularization term that penalizes tree complexity (Chen et al., 2016).

More generally, the boosting iteration itself can be understood as a form of regularization, where the effective model complexity grows with the number of boosting steps, motivating the use of explicit or implicit complexity control in boosting-type estimators (Bühlmann and Yu, 2003).

2.2.5. DT – CatBoost

This is a tree-based ML model that sequentially splits data according to input variables to generate a set of decision rules, where the final prediction is assigned at the terminal nodes that require no further

splitting (Ascari et al., 2023). Because DTs make predictions through explicit decision rules, they offer high interpretability and allow the rationale behind each prediction to be easily explained. However, a single DT often exhibits unstable performance and tends to overfit the training data (Aceña et al., 2022). To mitigate this limitation, ensemble approaches such as boosting employ multiple shallow trees to improve overall prediction accuracy and robustness.

In the present study, the CatBoost technique (a DT-based boosting approach) was adopted for model training. CatBoost is designed to handle categorical variables directly without requiring explicit preprocessing. To prevent information loss and data leakage that can occur when converting categorical features into numerical representations, CatBoost employs both the ordered boosting procedure and target statistics method (Jabeur et al., 2021). The ordered boosting procedure controls the training sequence so that, at each iteration, residuals and target statistics are computed using only preceding data, thereby preventing target leakage and reducing overfitting. Furthermore, CatBoost extends the conventional gradient boosting framework by incorporating a regularization term into its objective function and by naturally achieving model regularization through the boosting process (Zhang and Jánošík, 2024). A detailed mathematical derivation of the CatBoost technique can be found in (Prokhorenkova et al., 2018).

3. Methodology

3.1. Database description and model development

To elucidate the practical contribution of SAP characteristics to predicting the compressive strength of the resulting cementitious material, two models were defined in this study, as shown in Fig. 1. Model M1 was developed using variables based on both plain cementitious materials and SAP-incorporated cementitious materials data while excluding the SAP-related parameters (dosage amount, particle size, shape, type, and absorption capacity) from the input features. Subsequently, although M1 was trained using both plain and SAP-incorporated cementitious materials data, only the basic mix design variables were used as input features to establish a baseline prediction model. Model M2 was trained using only the SAP-incorporated cementitious materials data, in which the fundamental mix variables were supplemented with the specific characteristics of SAPs as additional

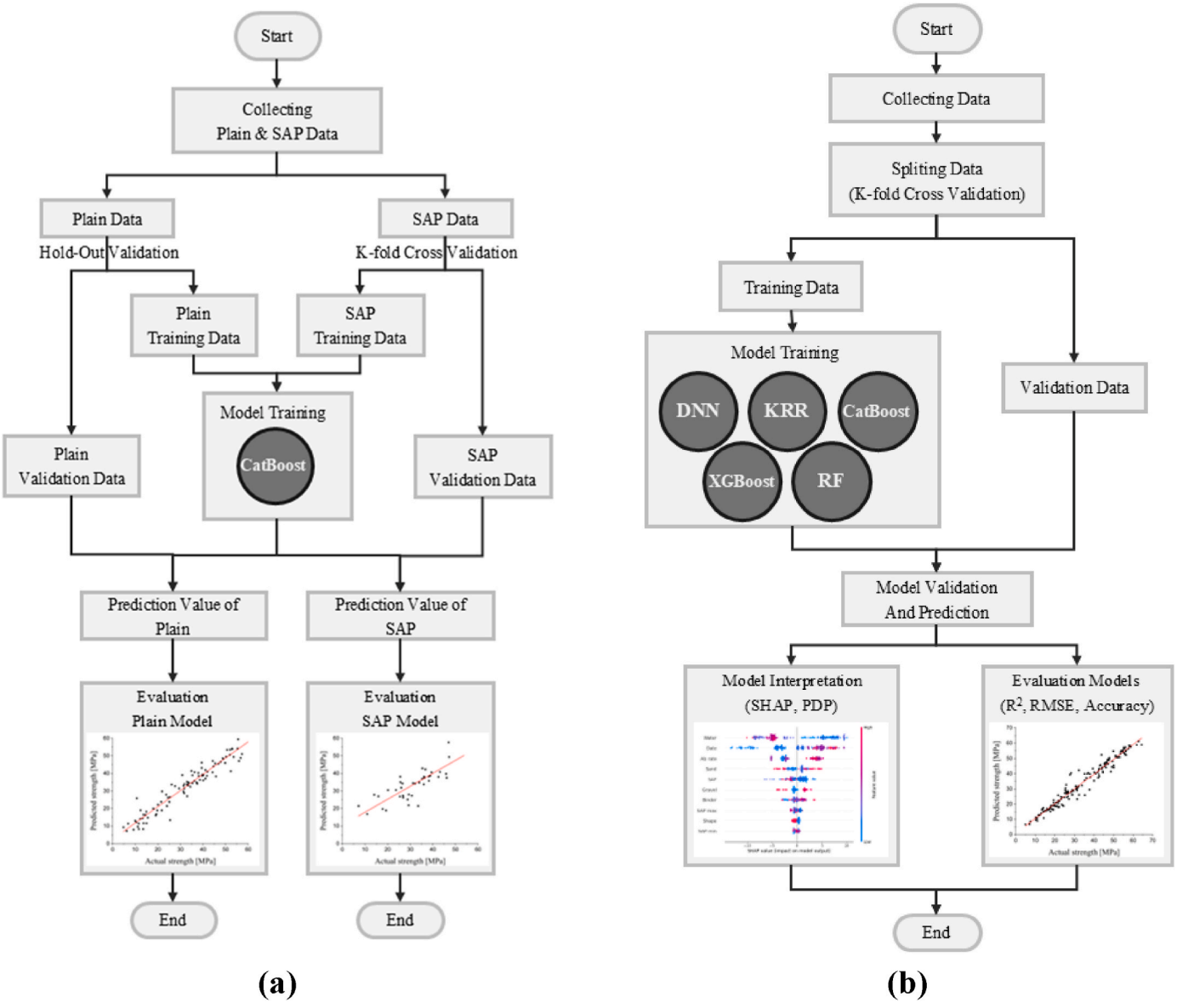


Fig. 1. Overall analysis workflows for ML models (a) M1 and (b) M2.

input features. In this case, five ML techniques: ANN, SVM, RF, XGBoost, and CatBoost were trained under identical preprocessing and data-splitting conditions to enable a performance comparison. The purpose of this comparison was to quantitatively determine the contribution of SAP characteristics to predicting the compressive strength of the resulting cementitious material. Details regarding data processing and evaluation procedures are described in the following sections.

3.1.1. Database development

The dataset used in this study was categorized into two groups. For M1, the plain cementitious materials data consisting of 1030 samples (including mix proportion variables and corresponding compressive strength values) were obtained from a publicly available dataset from the UCI Machine Learning Repository. This dataset covers a wide range of mix ratios and strength values, thereby making it suitable for training M1 and evaluating its performance on plain cementitious materials mixtures. Because the dataset for plain cementitious materials contains enough samples, the hold-out validation method was applied (i.e., dividing the data into 90% for training and 10% for testing). In contrast, the dataset for SAP-incorporated cementitious materials included only 40 samples, so K-fold cross-validation was employed to obtain a more reliable estimation of the predictive performance. In contrast to hold-out validation, K-fold cross-validation repeatedly partitions the data into multiple folds for iterative training and validation, which allows more efficient use of limited data. A schematic of the K-fold cross-validation procedure used in this study is shown in Fig. 2. The input features for M1 consisted of five variables (binder content, coarse aggregate content, fine aggregate content, water content, and curing age), while the output variable was the compressive strength.

The M2 prediction model was developed based on mix design data for SAP-incorporated cementitious materials, in which the intrinsic characteristics of SAPs were explicitly considered. A total of 171 samples of SAP-incorporated cementitious materials were extracted from previous studies and used for model training. Because of the limited dataset size, K-fold cross-validation was employed to reliably evaluate the model's generalization performance. The input features for M2 included the basic mix variables (binder content, coarse aggregate content, fine aggregate content, water content, and curing age) together with SAP-related parameters (SAP dosage amount, particle size, shape, type, and absorption capacity), while the output variable was the compressive strength. Notably, in the source studies, compressive strength is commonly reported as a mean value, sometimes accompanied by a standard deviation from replicate specimens. Because replicate-level measurements are generally not available in the published tables, each record in the M2 dataset corresponds to the reported mean strength for a given mixture/SAP condition, and the reported standard deviation was not used as an additional input. Accordingly, the trained model is intended to learn the central tendency across literature-reported cases, while specimen-to-specimen scatter is implicitly reflected as inherent experimental variability.

3.1.2. Data preprocessing and modeling

Because M1 and M2 use different sets of input variables, the collected data were preprocessed accordingly. First, to ensure consistency in input variables across the models, various types of binders (ordinary Portland cement, FA, and slag) were integrated into a single unified variable named *Binder*. Similarly, the coarse and fine aggregates were standardized and labeled as *Gravel* and *Sand*, respectively. Chemical admixtures such as water reducers and air-entraining agents were excluded from the inputs because their quantities were relatively small and their reported types and dosage amounts varied considerably among the sources, thus making a reliable quantitative comparison infeasible. In addition, the water content and curing age were encoded as *Water* and *Date*, respectively.

For the SAP-related parameters, the SAP dosage amount and absorption capacity were encoded as *SAP* and *Absorption capacity*, respectively. The particle morphology was denoted as *Shape*, with spherical particles encoded as 1 and irregularly shaped particles as 2. The *Type* variable representing the chemical composition of the SAP was encoded as 1 for sodium polyacrylate and 2 for acrylamide–acrylic acid copolymer. In the initial data curation stage, categorical descriptors such as *Shape* and *Type* were temporarily represented using simple integer codes (e.g., 1 and 2) to facilitate basic data inspection, distribution checks, and visualization. However, for model training, these variables were treated as nominal (non-ordinal) categorical features. To prevent the ML models from inadvertently learning artificial ordinal relationships from integer labels and to allow each category to be learned independently, one-hot encoding was applied. Accordingly, the *Shape* and *Type* variables were transformed into binary vectors with values in [0, 1], enabling the models to capture the distinct effects of

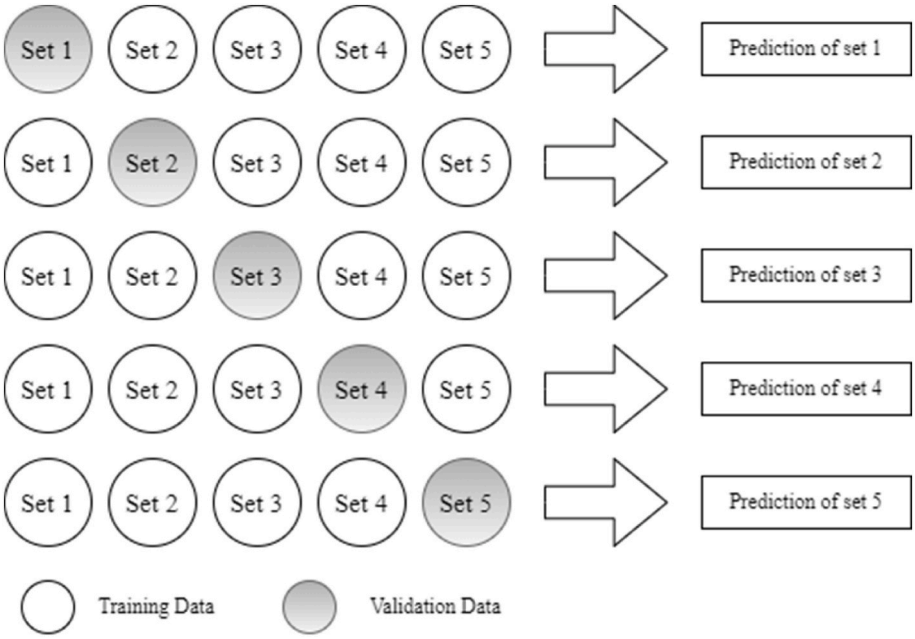


Fig. 2. A schematic of the K-fold cross-validation procedure used in this study.

SAP particle shape and chemical type on compressive strength prediction.

The distribution of 171 data points comprising the mix design parameters, SAP characteristics, and compressive strength values extracted from eight published studies is presented as histograms in Fig. 3 (Dang et al., 2017; Hong et al., 2019, 2024; Chindasiriphan et al., 2020; Xu et al., 2022; Beushausen et al., 2014; Patil et al., 2023; Yao et al., 2024). As shown in Fig. 3, categorical variables such as SAP type and shape are not perfectly balanced across levels. In general, imbalance effects depend not only on class-count ratios but also on data complexity (e.g., overlap and representativeness) (He and Garcia, 2009). In the present dataset, the categorical distributions are skewed to some extent, but they do not appear to be extremely dominated by a single level. In practical ML model development, an imbalance of this magnitude is often considered manageable and is less likely to be the primary driver of model behavior (He and Garcia, 2009; Krawczyk, 2016); thus, the influence on overall model performance and the main interpretation of feature effects is expected to be limited. Still, generalization to under-represented levels may involve additional uncertainty, and future work should expand minority-level data and assess category-wise performance. Correlations among the variables are shown as a Pearson's correlation matrix in Fig. 4. The matrix represents the degree and direction of linear relationships between the variables quantified by using Pearson's correlation coefficient: values close to $+1$ and -1 indicate strong positive and negative linear correlations, respectively, while those near 0 suggest weak or no linear correlation. It is noteworthy that some variables, such as SAP dosage amount and absorption capacity, can still exert a substantial influence on compressive strength even when their Pearson's correlation coefficient values are relatively low, which can be attributed to nonlinear relationships or interactions among the variables.

To account for cross-study heterogeneity that can affect compressive

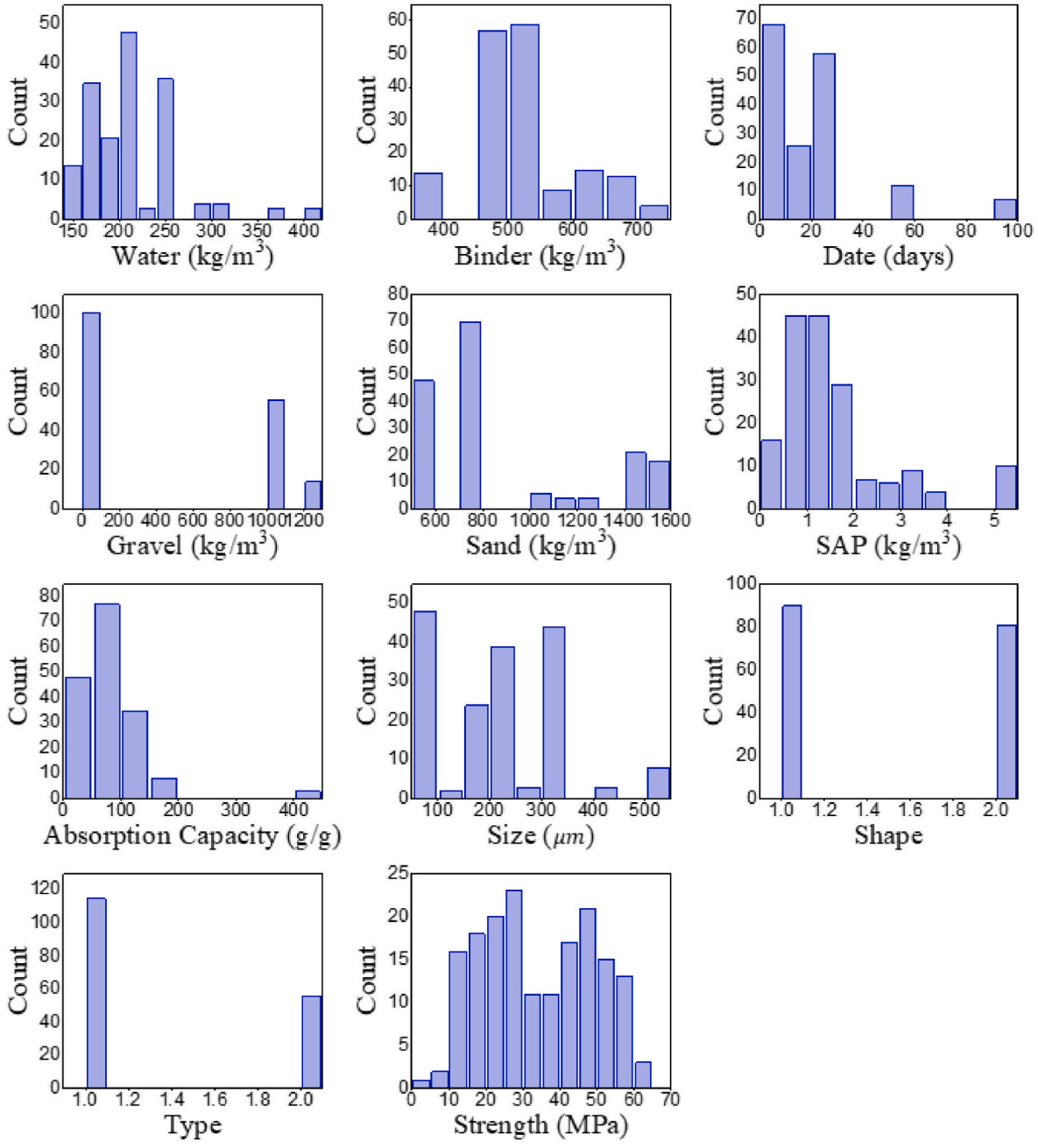


Fig. 3. Distributions of the variables in the SAP-incorporated cementitious materials dataset.

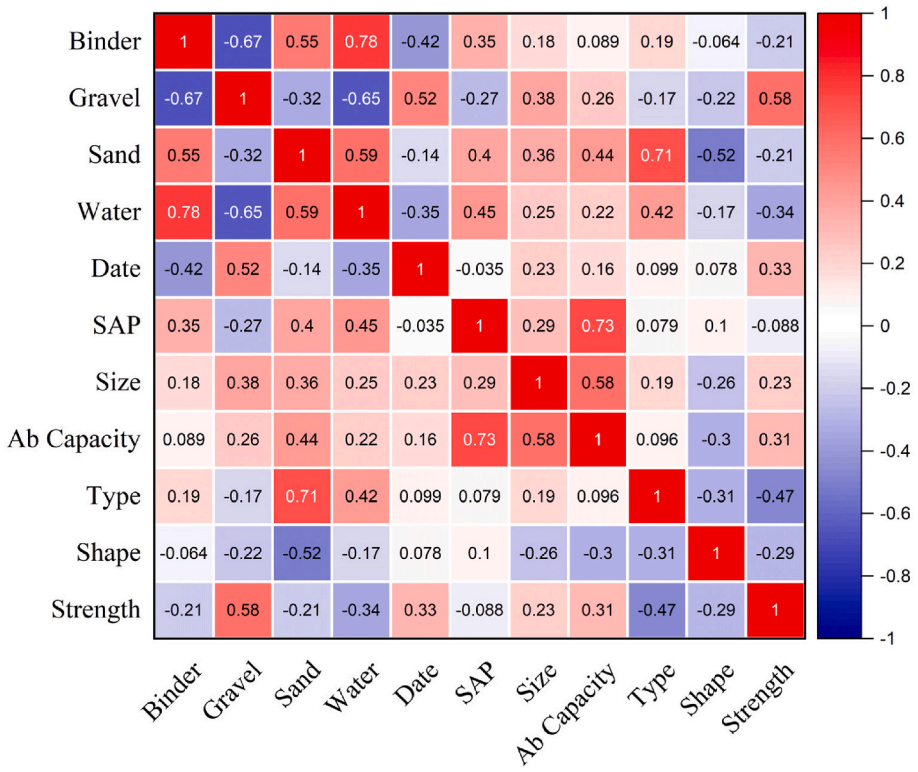


Fig. 4. Pearson's correlation matrix for the SAP-incorporated cementitious materials dataset. Ab, absorption.

strength, the curing conditions and the geometry/dimensions of compressive-strength specimens reported in the source studies were compiled and summarized in Table 1. Variations in specimen shape (cube vs. cylinder) and dimensions, as well as curing temperature, relative humidity, and curing environment, are known to influence measured compressive strength even for similar mixtures (Rosa and Ruiz, 2025; Yi et al., 2006). Among these factors, specimen shape was prioritized for normalization because it can introduce systematic differences across studies while allowing an explicit conversion. Accordingly, cube-reported strengths were converted to equivalent cylinder strengths using an approximate cylinder-to-cube ratio of 0.8, consistent with the European strength class convention adopted in Eurocode 2 (European Committee for Standardization (CEN), 2021; Narayanan, 2024), whereas cylinder-reported strengths were retained without conversion, enabling consistent comparison within a unified cylinder-based strength framework. Nevertheless, as indicated in Table 1, differences in curing regimes and detailed specimen dimensions may still contribute to residual inter-study variability (Yi et al., 2006; Al-Gahtani, 2010; Sun et al., 2021). Because these factors are reported under diverse protocols and are not readily amenable to a single harmonization rule, they were not normalized beyond the cube-to-cylinder conversion and should be regarded as an inherent limitation of literature-aggregated datasets. Future work should expand datasets generated under more standardized protocols, incorporate curing method-related descriptors more explicitly, and account for study-level heterogeneity to further improve robustness and generalizability.

Finally, to compare the performances of different ML techniques within M2, five algorithms (DNN, KRR, RF, XGBoost, and CatBoost) were implemented in Python under identical preprocessing and data-splitting conditions. Notably, three tree-based models (RF, XGBoost, and CatBoost) were included to represent complementary tree-ensemble paradigms, namely bagging and gradient boosting, and to examine how differences in regularization and categorical-feature handling strategies influence predictive performance under the same evaluation protocol. In addition, hyperparameters were tuned using a search-based procedure under the same cross-validation protocol used for model evaluation. For each technique, a set of candidate hyperparameter combinations was explored (grid/random search depending on the model), and the final configuration was selected based on the lowest validation RMSE averaged over the cross-validation folds. Unless otherwise specified, non-listed hyperparameters were kept at their library defaults. The resulting hyperparameter settings are summarized in Table 2.

Table 1
Curing conditions and geometry of the ML datasets.

Reference	Curing method		Specimen geometry [mm]	Strength conversion factor
	Temperature [°C]	Relative humidity [%]		
Dang et al. (Dang et al., 2017)	20 ± 2	95	150 × 150 × 150	0.8
Hong et al. (Hong et al., 2019)	20 ± 1	100	50 × 50 × 50	0.8
Chindasiriphan et al. (Chindasiriphan et al., 2020)	—	100	Ø100 × 200	—
Hong et al. (Hong et al., 2024)	23 ± 1	100	50 × 50 × 50	0.8
Xu et al. (Xu et al., 2022)	20 ± 2	98	40 × 40 × 40	0.8
Beushausen et al. (Beushausen et al., 2014)	23 ± 2	50 ± 5	100 × 100 × 100	0.8
Patil et al. (Patil et al., 2023)	—	100	150 × 150 × 150	0.8
Yao et al. (Yao et al., 2024)	20 ± 2	95	100 × 100 × 100	0.8

Table 2
Hyperparameter configurations of the ML techniques.

Technique	Hyperparameter
DNN	Hidden layers = 6; Nodes per layer = 256; Learning rate = 0.001; Epochs = 1000
KRR	Kernel = rbf; Alpha = 0.001; Gamma = 1
RF	N estimators = 1000; N jobs = −1
XGBoost	N estimators = 5000; Learning rate = 0.01; Max depth = 4
CatBoost	Iterations = 500; Learning rate = 0.01; Depth = 4; Loss function = RMSE

3.2. Model assessment

3.2.1. Performance evaluation indicators

In this study, the performance of the models was evaluated using R^2, mean squared error (MSE), root MSE (RMSE), and prediction accuracy respectively calculated as follows:

$$R^2 = 1 - \frac{\sum_{i=1}^{n}(y_i - \hat{y}_i)^2}{\sum_{i=1}^{n}(y_i - \bar{y})^2}, \tag{7}$$

$$\mathrm{MSE} = \frac{1}{n}\sum_{i=1}^{n}(y_i - \hat{y}_i)^2, \tag{8}$$

$$\mathrm{RMSE} = \sqrt{\frac{1}{n}\sum_{i=1}^{n}(y_i - \hat{y}_i)^2}, \tag{9}$$

$$\text{MAPE based accuracy}(\%) = 100 - \mathrm{MAPE} = 100\left(1 - \frac{1}{n}\sum_{i=1}^{n}\frac{|\hat{y}_i - y_i|}{y_i}\right), \tag{10}$$

where y_i denotes the actual value, $\hat{y}_i$ is the predicted value, and $\bar{y}$ is the mean of the actual values. R^2 represents the proportion of variation in the actual data that is explained by the model: a value closer to 1 indicates higher explanatory power, MSE is the mean of the squared differences between the predicted and actual values, RMSE represents the average magnitude of prediction errors on the same scale as the actual data, and MAPE based accuracy is an error-derived metric defined based on MAPE, and values closer to 100% indicate higher predictive accuracy with smaller average relative error between predicted and actual values. This metric is used to provide an intuitive, percentage-based summary of relative prediction error (Liu et al., 2024; Kilimci et al., 2019).

3.2.2. Model interpretability

Although ML-based predictive models are capable of effectively capturing complex nonlinear relationships and multidimensional interactions among variables, they often suffer from limited interpretability. In particular, when the input variables represent physically meaningful material properties, it is essential to employ interpretability tools that can provide transparent explanations of how the model operates and how each variable influences the prediction outcomes. Therefore, in the present study, SHapley Additive exPlanations (SHAP) analysis was employed together with the Partial Dependence Plot (PDP) and Individual Conditional Expectation (ICE) methods, all of which are widely used for interpreting and visualizing feature contributions in ML models.

SHAP is a representative post-hoc interpretability method for quantitatively explaining the predictions of ML models (Retzlaff et al., 2024). It quantifies the contribution of each input variable, thereby presenting feature importance and the direction of influence in a fair and intuitive manner. This method is based on cooperative game theory (specifically the concept of the Shapley value), which theoretically guarantees that the contribution of each feature within a predictive model is allocated in an axiomatic and theoretically consistent manner (Lundberg et al., 2017). Specifically, SHAP evaluates how the model output changes with respect to each input by aggregating the marginal contributions across all possible feature subsets (Štrumbelj and Kononenko, 2010). As a result, it provides a unique additive feature attribution that satisfies the properties of consistency, missingness, and local accuracy (Neubauer et al., 2025). Owing to these characteristics, SHAP enables the quantitative and comprehensive interpretation of the internal workings of complex ML models (Ali et al., 2023). The feature contribution in SHAP is calculated as follows:

$$\varphi_i(x) = \sum_{S \subseteq F \setminus \{i\}} \frac{|S|!(|F| - |S| - 1)!}{|F|!}\left[f_{S\cup\{i\}}(x_{S\cup\{i\}}) - f_s(x_s)\right], \tag{11}$$

where $\varphi_i(x)$ denotes the contribution of feature i to the prediction for input x, F represents the set of all features, and S denotes any subset of F that does not include i (Cavaleri et al., 2022).

PDP is a representative post-hoc interpretability method designed to visualize and quantitatively interpret the average marginal effect of a specific variable or set of variables on the predictions generated by ML models. It estimates the effect of a target variable by fixing its value and averaging the predicted outcomes over the marginal distributions of all other variables (Apley and Zhu, 2020). However, because PDP does not account for the heterogeneity of individual observations, it may overlook nonlinear dependencies or feature interactions within the data (Molnar et al., 2022). To address this limitation, the ICE method was introduced, which examines the model's response at the level of individual observations by varying the value of a target feature while holding the observed values of all other features constant. Each ICE plot produces one curve per observation; this enables detailed examination of variations in prediction sensitivity across observations, as well as evidence of feature interactions and nonlinear response patterns, thereby complementing the global trends revealed by PDP (Goldstein et al., 2015). Consequently, ICE curves provide a localized interpretation of how the model predictions vary with changes in feature values, thereby enriching the global summary offered by PDP with fine-grained, instance-level insights (Huang et al., 2023).

This study also utilized the difference between the maximum and minimum predicted values obtained from the PDP curves for each variable. This metric was employed not only to capture the average trend of the curve but also to quantitatively evaluate the extent to which each variable influences the absolute range of model outputs: a larger difference between the maximum and minimum values indicates a wider variation in the model predictions induced by that variable, thereby providing supplementary insights into the relative importance and sensitivity of the features within the model.

3.3. Experimental investigation

An experimental investigation was conducted to complement the ML-based analysis and further examine the effects of SAP characteristics on compressive strength. This approach was intended to cross-validate the data-driven interpretations and provide deeper insights into the findings. Specifically, cementitious specimens were prepared with varying SAP dosage amounts, shapes, and types. In addition to compressive strength testing, the pore characteristics (reported in numerous previous studies to have a significant influence on strength) were analyzed using X-ray micro-CT.

3.3.1. Materials and mix design

The cement used in this study was Type I ordinary Portland cement conforming to ASTM C150/C150M (ASTM International, 2024) (its chemical composition is provided in Table 3), while standard sand complying with ISO 679 (International Organization for Standardization (ISO), 2009) was used as the fine aggregate. The SAPs used in this study were sodium polyacrylate and acrylamide–acrylic acid copolymer with

Table 3
Chemical composition of Type I ordinary Portland cement.

CaO	SiO_2	Al_2O_3	Fe_2O_3	MgO	SO_3	K_2O	Na_2O	LOI[a]
61.80	20.50	4.97	3.02	2.71	2.35	0.72	0.33	2.36

[a] Loss on ignition. All values are expressed as mass%.

irregular (Fig. 5a) and spherical (Fig. 5b) particle shapes, respectively. The mix proportions are summarized in Table 4. The SAP dosage amount, particle shape, or type was designated as the main factor depending on the objectives of the experimental program. The water-to-cement ratio was adjusted to achieve a flow of 180 ± 10 mm, as measured via flow testing conducted immediately after mixing in accordance with ASTM C1437 (ASTM International, 2020).

3.3.2. Testing methods

This experimental investigation was designed to evaluate whether incorporating SAP characteristics into the porosity–compressive strength relationship based on the Balshin equation (Balshin, 1949) could improve its predictive performance. For this purpose, the 28-day compressive strength of each specimen was measured, and the porosity was determined from a region of interest (ROI) with an identical volume. Using these data, both the original Balshin equation (Balshin, 1949) and an extended equation incorporating SAP characteristics were established and applied to compare their predictive accuracy. Compressive strength testing was conducted on 50 × 50 × 50 mm cubic specimens after 28 days of curing at 20 °C and 100% relative humidity, in accordance with ASTM C109 (Lorenzoni et al., 2020).

After curing for 28 days, X-ray micro-CT scanning was performed on cylindrical disks (diameter: 9 mm; height: 10 mm) cut from each mixture specimen. The scans were conducted using an X-ray micro-CT system (Skyscan1172, Bruker Corp., Billerica, MA, USA) under the following conditions: source voltage of 100 kV, source current of 100 μA, and voxel size of approximately 12 μm. The acquired 2D images were reconstructed and analyzed using 3D visualization and analysis software (Dragonfly 3D World, Object Research Systems [ORS] Ltd., Montreal, Canada). As shown in Fig. 6, an ROI of identical volume was extracted from each scanned specimen, and segmentation was performed to classify normal pores, SAP voids (pores formed due to SAP shrinkage), and SAP particles.

Because the grayscale distribution of SAP particles nearly overlaps with that of the mortar matrix and the SAP voids exhibit the same brightness level as normal pores, distinguishing these phases is challenging. Although they can be differentiated by shape, boundary continuity, and local context, manual segmentation is time-consuming and susceptible to operator bias, thus making consistent comparisons difficult. Therefore, to ensure fairness and efficiency in segmentation, a U-Net-based semantic segmentation approach was adopted in the present study by following previously reported protocols (Lorenzoni et al., 2020; Chen et al., 2022). The deep-learning parameters used for training are summarized in Table 5, and the training process was implemented within Dragonfly 3D World. An example of the segmentation results obtained by applying the trained model to the original 2D CT image is shown in Fig. 7.

Table 4
Mixture proportions for the specimens.

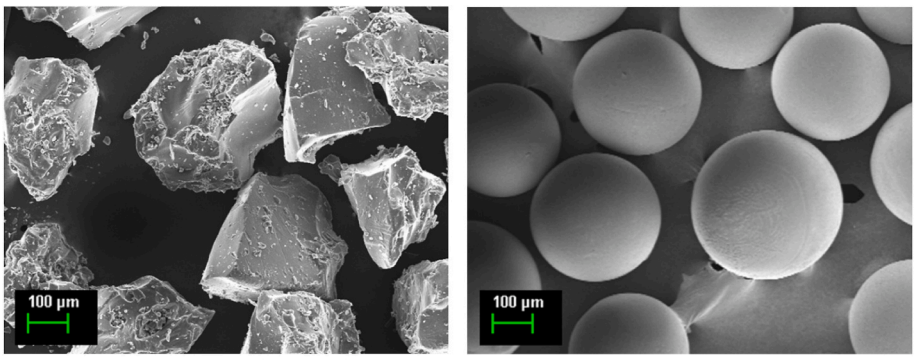
Specimen	Cement [kg/m^3]	Fine Aggregate [kg/m^3]	Water [kg/m^3]	SAP A[a] [kg/m^3]	SAP B[b] [kg/m^3]
#1	1498.2	—	524.4	—	—
#2	678.8	1154.0	339.4	—	—
#3	1498.2	—	599.4	7.5	—
#4	655.2	1113.8	360.4	3.3	—
#5	1498.2	—	674.4	15.0	—
#6	633.2	1076.4	379.9	6.3	—
#7	602.2	1023.7	409.5	—	6.0
#8	1498.2	—	749.4	22.5	—

[a] Sodium polyacrylate.
[b] Acrylamide–acrylic acid copolymer.

4. Results and discussion

4.1. M1 performance

M1 was trained using an integrated dataset comprising both plain and SAP-incorporated cementitious materials mixtures, while excluding SAP characteristics from the input variables. Fig. 8 presents the scatter plots of the predicted and actual compressive strength values, and Table 6 summarizes the corresponding performance indicators. For the plain cementitious materials dataset, the R^2 and accuracy were 0.9397 and 87.34%, respectively, indicating that the model explained most of the data variance. In contrast, for the SAP-incorporated cementitious materials dataset, these values decreased markedly to 0.6513 and 79.94%, respectively. Moreover, the MSE and RMSE for the SAP-incorporated cementitious materials increased by 115.4% and 46.7%, respectively, compared with those for plain cementitious materials, quantitatively demonstrating that not only the correlation but also the error magnitude increased substantially. This performance gap can be interpreted as a consequence of altered strength development mechanisms in SAP-modified concrete. SAP incorporation modifies moisture transport, pore formation, and hydration pathways, such that internal curing, SAP-induced voids, and changes in hydration collectively influence compressive strength even under identical conventional mix design variables. Consequently, the SAP-incorporated cementitious materials exhibited a distinct strength development behavior compared with the plain cementitious materials, and using the input variables for the latter only was insufficient to accurately predict the compressive



(a) (b)

Fig. 5. Scanning electron microscopy images of SAPs (a) sodium polyacrylate and (b) acrylamide–acrylic acid copolymer.

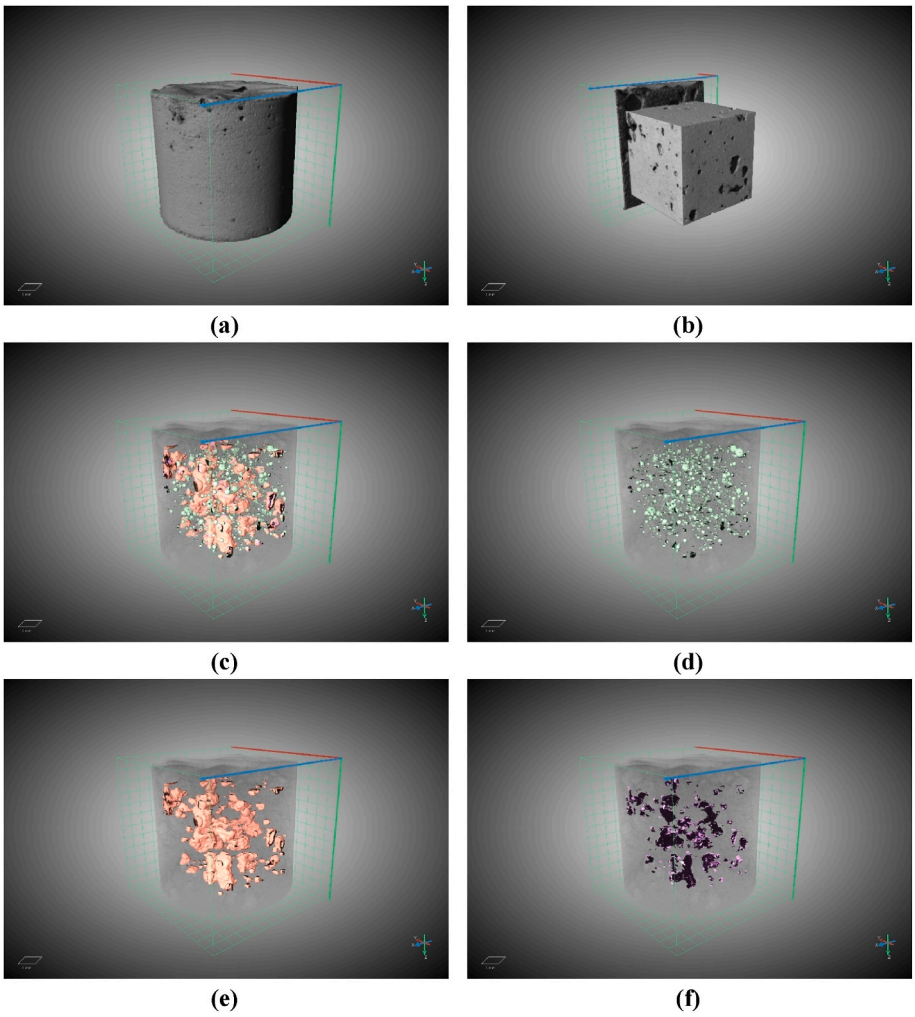


Fig. 6. X-ray micro-CT analysis workflow in Dragonfly: (a) 3D reconstruction; (b) region of interest selection/cropping; (c) multiclass segmentation overlay (normal pores, SAP voids and particles); and isolated (d) normal pores, (e) SAP voids, and (f) SAP particles.

Table 5
Deep-learning parameters for U-Net-based semantic segmentation.

Parameter	Setting
Patch size (pixels)	64 × 64
Stride ratio	0.25
Batch size	256
Epochs	100
Loss function	Categorical cross-entropy
Optimizer	Adadelta
Learning rate	1.0
Data augmentation	H/V[a] flips; rotation 180°; zoom 0.9–1.1; shear 2.0°; factor × 10[b]

[a] Horizontal/vertical.
[b] Augmentation factor.

strength. These results indicate that the accurate prediction of compressive strength in SAP-incorporated cementitious materials requires dedicated models built upon datasets and input frameworks that explicitly incorporate SAP characteristics.

4.2. M2 performance

4.2.1. Comparison among DNN, KRR, RF, XGBoost, and CatBoost

For the M2 model, five ML techniques (DNN, KRR, RF, XGBoost, and CatBoost) were applied under identical preprocessing and data-splitting conditions for performance comparison. Fig. 9 presents scatter plots of the predicted and actual compressive strength values for each technique, while Table 7 summarizes their corresponding performance metrics. Overall, the CatBoost-based M2 achieved the best predictive performance, followed by XGBoost and RF, whereas KRR and DNN showed progressively lower accuracy. Specifically, CatBoost yielded the highest coefficient of determination ($R^2 = 0.9680$) and the lowest error levels (MSE = 4.443; RMSE = 2.108), together with the highest MAPE based accuracy (92.70%). A quantitative comparison shows that the RMSE of the CatBoost-based M2 was 62.5% lower than that of the DNN-based M2 and 57.4% lower than that of the KRR-based M2, indicating a substantial reduction in absolute prediction error. This performance gap can be interpreted by considering both the characteristics of the M2 dataset and the learning mechanisms of each model. The M2 dataset has a relatively limited sample size and simultaneously includes continuous mix-proportion variables and categorical SAP descriptors (e.g., type and shape); under such conditions, tree-based learners can be advantageous (Shwartz-Ziv and Armon, 2022).

In particular, DT-based models can naturally capture threshold-like nonlinear behavior and higher-order inter-variable interactions by approximating the input space via piecewise partition rules, making them structurally suitable for problems dominated by multivariate coupling effects, such as compressive strength (Wickramarachchi et al., 2016). In contrast, although DNNs have high representational capacity, they involve many trainable parameters, which increases the risk of

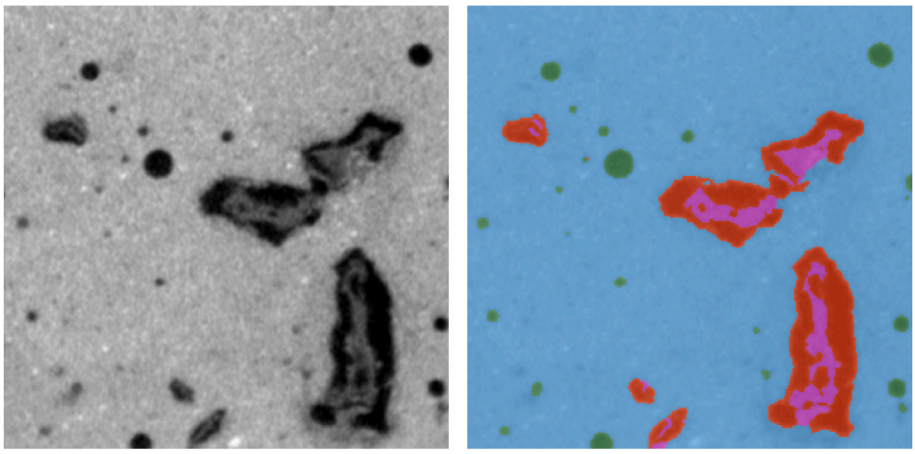


Fig. 7. Example results from the U-Net-based segmentation model: (a) the original 2D X-ray micro-CT slice and (b) the segmentation output (blue: mortar matrix; green: normal pores; red and violet: superabsorbent polymer voids and particles, respectively).

overfitting under small-sample conditions and can heighten reliance on strong regularization and tuning for stable generalization (Khan et al., 2019). Moreover, while KRR can model nonlinear relationships through kernels, it inherently relies on a global, smooth approximation; thus, when the data do not sufficiently support local structures, it may fail to adequately reflect localized interaction patterns or threshold-like behavior (Zheng et al., 2010). Therefore, under conditions such as those of M2 in this study, namely a small sample size, mixed-type inputs, and an interaction-/nonlinearity-dominated structure, DT-based ensembles can lead to more stable and accurate predictive performance than DNN and KRR.

Furthermore, among tree-based ensembles, the superior performance of CatBoost over RF and XGBoost can be explained by differences in the learning paradigm and in mechanisms for handling categorical variables and stabilizing generalization. RF, as a bagging-based technique, trains multiple trees in parallel and excels at reducing variance; however, because it does not sequentially correct residuals as boosting does, it may achieve less bias reduction in complex nonlinear and interaction-rich structures (Friedman, 2002; Petersen et al., 2007). In contrast, Gradient Boosting Decision Trees (GBDTs) accumulate shallow trees and sequentially correct pseudo-residuals at each stage, which is advantageous for interaction-dominated problems (Friedman, 2002). While both XGBoost and CatBoost belong to the GBDT family, they differ in how categorical variables are handled. XGBoost typically learns after categorical variables are numerically encoded via external preprocessing such as one-hot encoding, whereas CatBoost internally processes categorical variables using target-statistics-based approaches and is designed to mitigate prediction shift due to target leakage via ordered boosting, which can yield more stable generalization under small-sample settings with categorical inputs (Hu et al., 2025; Chelgani et al., 2023). These algorithmic differences are consistent with the performance patterns observed in Table 7. Similar trends have been reported in comparative studies, where CatBoost often performs strongly relative to other tree-based alternatives, suggesting that such design choices can translate into performance gaps.

To evaluate the generalization capability of M2 beyond the training domain, model performance was additionally examined using an independent external test dataset. The external dataset consisted of 22 SAP-incorporated cases collected from two published studies (Arckarapunyathorn et al., 2025; Al-Shawafi et al., 2024), together with additional experimental data generated in this study; notably, the latter included cement paste-based specimens. These external data were strictly excluded from model training and cross-validation and were used only after all models under the M2 setting had been fully developed. Table 8 presents the predictive performance of each technique on the external test dataset. The tree-based ensemble techniques (RF, XGBoost, and CatBoost) showed consistently strong performance at a comparable level on the external data. The average RMSE of these three techniques was 9.49, and the MAPE based accuracy was 82.53%, indicating relatively stable predictive performance under external conditions. In contrast, KRR exhibited the lowest performance, with an RMSE of 24.55 and an accuracy of 40.18%. Because the external test data were drawn from different sources and included conditions not represented in the training dataset (including cement paste-based specimens), some performance degradation and changes in the relative ranking of techniques were observed compared with the training-dataset results in Table 7. Nevertheless, the tree-based ensemble techniques maintained relatively stable robustness under these distribution shifts. Given that the external test dataset size is limited, future work should further validate generalization performance using a larger external dataset that covers a wider range of material systems and more standardized testing conditions.

4.2.2. *Comparison with existing predictive models*

To more clearly assess the comparative performance of the CatBoost-based M2, which exhibited the best performance in Section 4.2.1, an additional comparison was conducted with predictive models reported in previous studies on SAP-incorporated cementitious materials. In the literature, strength prediction for SAP-incorporated systems varies across studies in terms of the prediction target (e.g., absolute compressive strength, relative strength, or strength degradation) as well as the set of input variables. Therefore, there are practical limitations in directly comparing all literature models under exactly the same conditions as those adopted in this study. In this context, the study selected prior studies that explicitly addressed strength prediction of SAP-incorporated cementitious materials and reported both the predictive model and its performance metrics. To ensure representativeness of modeling approaches, the selected models were classified into three categories: (i) an empirical regression-based model (Ding et al., 2017), (ii) analytical (physics-based) model (Zhao et al., 2022), and (iii) a ML-based model (Hosseinzadeh et al., 2024). For each category, the reported performance level, applicability, and major constraints were discussed. Where applicable, CatBoost-based M2 was compared with these models using consistent evaluation metrics to discuss its engineering applicability. Table 9 summarizes the performance metrics reported in the literature together with those obtained for the proposed model in this study.

The empirical regression model (Ding et al. (2017)) provides

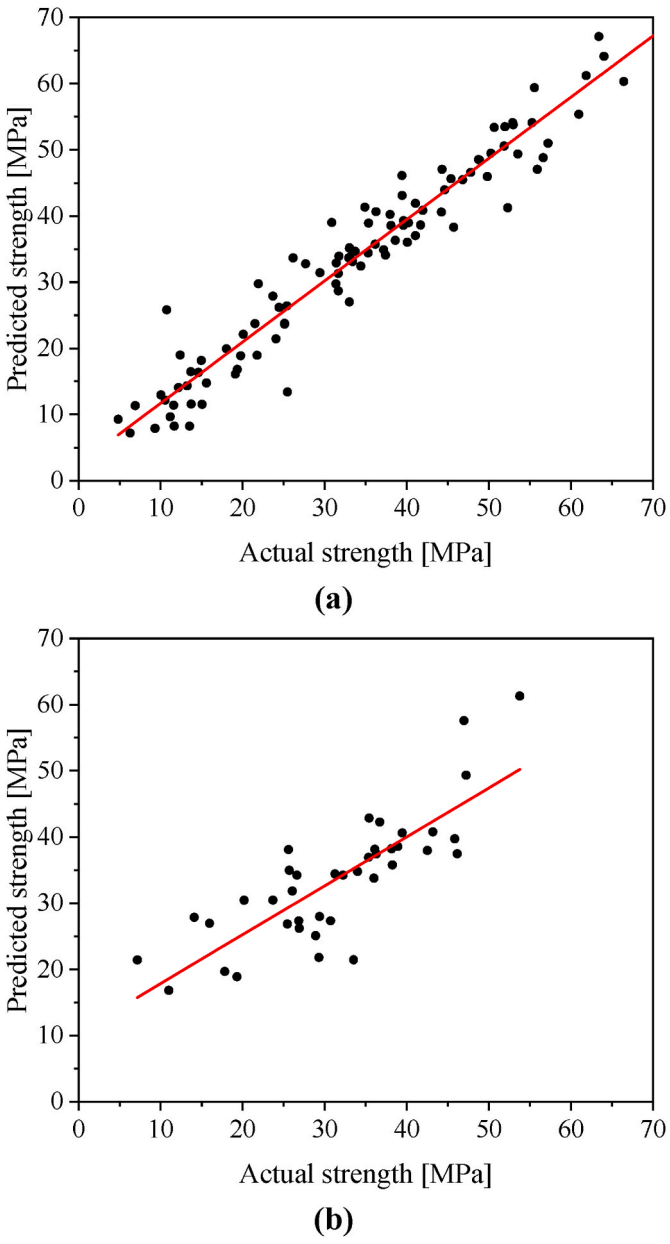


Fig. 8. M1-predicted vs. actual compressive strengths of (a) the plain concrete and (b) SAP-incorporated concrete samples. The red line indicates least-squares fitting of the data.

Table 6
Compressive strength predictive performance using M1 on plain and SAP-incorporated concrete datasets.

Dataset	R^2	MSE	RMSE	MAPE based Accuracy
Plain	0.9397	14.76	3.842	87.34
SAP-incorporated	0.6513	31.79	5.638	79.94

closed-form relationships for age-dependent compressive strength using a limited set of variables such as SAP dosage and particle size. This enables rapid estimation and trend identification under identical or comparable test conditions. However, because this formulation relies on a multiple linear regression formulation and does not explicitly represent intrinsic SAP characteristics such as shape, type, and absorption capacity, its ability to capture nonlinear interactions and maintain generalizability may decrease when the application domain changes (e.g., different mixture conditions or SAP systems). The analytical (physics-based) model (Zhao et al. (2022)) adopts a mechanism-informed formulation to describe relative strength (Q) by considering internal curing effects and SAP-induced void/air contributions, which is beneficial for interpreting how SAP influences strength. In contrast, the model requires a reference mixture strength and additional parameters linked to SAP absorption characteristics. Therefore, applying the model in practice may require defining an appropriate reference mixture and estimating the necessary input parameters, which can increase the implementation effort. The ML-based model (Hosseinzadeh et al. (2024)) uses literature-derived data to predict strength reduction (SR). Its application typically requires reference-strength information, and limited representation of intrinsic SAP characteristics (type, shape, absorption capacity) may constrain discrimination across SAP systems. In contrast, the CatBoost-based M2 developed in this study targets absolute compressive strength and explicitly incorporates multi-dimensional intrinsic SAP characteristics (particle size, shape, type, and absorption capacity) in addition to mixture variables. As summarized in Table 9, CatBoost-based M2 achieved an R^2 of 0.968 (RMSE = 2.11) for absolute compressive strength prediction, whereas the reported ML performance in the literature is $R^2 = 0.86$–0.89 for strength reduction prediction, reflecting the combined effect of the enriched SAP feature set and the suitability of CatBoost for handling nonlinear interactions. Overall, while the representative models considered here are useful for rapid estimation (regression), mechanism-based interpretation (analytical model), and prediction of a degradation-related index (ML model), the present study offers a practical approach for absolute compressive strength prediction that quantitatively reflects the role of intrinsic SAP characteristics.

4.3. Feature importance analysis

As confirmed in Section 4.2, CatBoost-based M2 exhibited the best predictive performance. Based on this, the model's internal workings were interpreted and the effects of the principal variables were quantitatively analyzed. According to SHAP results for CatBoost-based M2 presented in Fig. 10, *Water* and *Date* were identified as the most influential variables contributing to the predicted compressive strength: *Water* exhibited higher SHAP values concentrated in the negative region, indicating that increasing the water content tended to decrease the predicted compressive strength, whereas *Date* showed higher SHAP values in the positive region, suggesting that increasing the curing age positively influences compressive strength development. In particular, the contribution of *Date* displayed a nonlinear increasing trend beyond a certain threshold. Among the SAP-related features, *SAP*, *Absorption capacity*, and *Type* also made notable contributions to the model predictions, which supports the interpretation that the presence and physicochemical properties of SAPs significantly affect the compressive strength of the resulting cementitious materials.

Fig. 11 shows a comparison of the range of predicted compressive strength values obtained from the PDPs for each input variable: a larger range indicates a greater absolute influence of the corresponding variable on the model output. It can be seen that *Water* and *Date* exhibited the largest variation ranges of 15.86 and 15.62 MPa, respectively, confirming that these two variables are predominant factors governing compressive strength. Among the SAP-related features, *Absorption capacity* and *SAP* showed notable variation ranges of 6.47 and 4.90 MPa, respectively, indicating that they are major influencing factors. In contrast, *Size* (0.86 MPa) and *Shape* (0.16 MPa) exhibited small variation ranges, suggesting that their relative influence was negligible within the scope of this study. Overall, these findings quantitatively confirm that while *Water* and *Date* play predominant roles in the prediction of compressive strength, the SAP-related characteristics also contribute substantially.

The PDP and ICE results for the SAP-related variables are shown in Fig. 12. It can be seen that the predicted compressive strength gradually

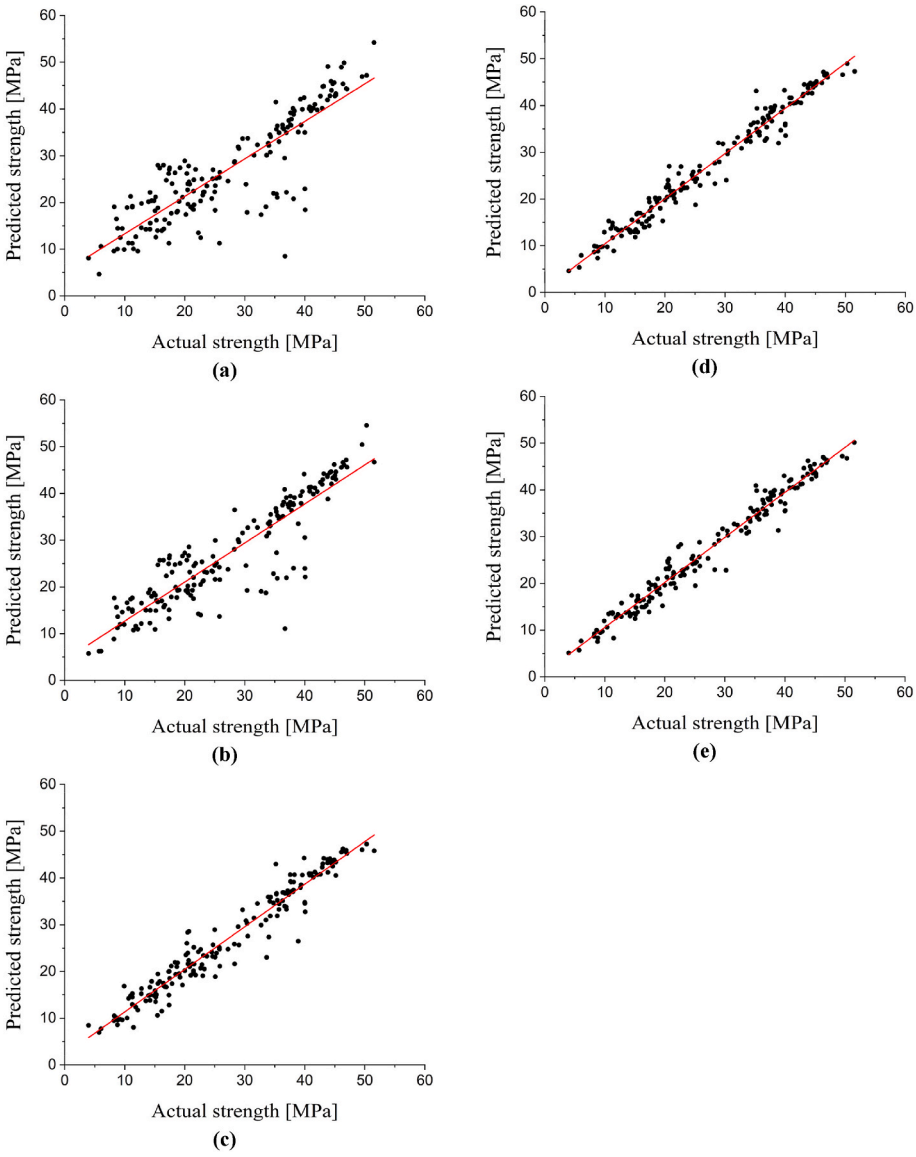


Fig. 9. M2-predicted vs. measured compressive strength of concrete using the SAP-incorporated concrete dataset and (a) DNN, (b) KRR, (c) RF, (d) XGBoost, (e) CatBoost. The red line indicates least-squares fitting of the data.

Table 7
Predictive performance of M2 using the five ML techniques and the SAP-incorporated concrete dataset.

Technique	R^2	MSE	RMSE	MAPE based Accuracy
DNN	0.7466	31.53	5.615	80.12
KRR	0.8045	24.52	4.952	83.67
RF	0.9396	7.724	2.779	89.78
XGBoost	0.9666	4.662	2.159	92.61
CatBoost	0.9680	4.443	2.108	92.70

Table 8
Predictive performance of M2 on the external SAP-incorporated concrete test dataset using five ML techniques.

Technique	MSE	RMSE	MAPE based Accuracy
DNN	233.6	15.28	67.05
KRR	602.9	24.55	40.18
RF	48.77	6.984	84.33
XGBoost	104.1	10.20	81.21
CatBoost	127.1	11.27	82.06

decreased with increasing water content. This is as expected because an increase in the effective water-to-cement ratio raises the amount of residual water after hydration, thereby increasing porosity and reducing compressive strength. A stepwise drop was observed at around 200 kg/m^3, which may be attributed to localized data clustering or exaggerated localized discontinuities resulting from the piecewise partitioning nature of the tree-based model. This is plausible because the SAP-incorporated cementitious materials dataset contains a limited number of samples that are unevenly distributed across certain regions. Binder content was positively correlated with compressive strength and showed a gradual increase up to approximately 550–600 kg/m^3, beyond which a plateau region was observed in its profile. Meanwhile, the slopes for both fine and coarse aggregates are relatively gentle and approach the upper limit beyond a certain content range.

SAP dosage amount exhibited a positive effect on compressive strength up to a certain threshold, beyond which excessive incorporation led to a reduction. This behavior was interpreted as the point at which the influence of SAP voids formed after water release becomes predominant. Further discussion on this phenomenon is provided in Section 4.4.

Table 9
Comparison of representative predictive models for SAP-incorporated cementitious materials.

Approach	Reference	Prediction target	SAP-related inputs	Performance	Remarks
Empirical regression	Ding et al. (Ding et al., 2017)	f_c (3, 7, 28 d)	dosage, particle size	Adj. $R^2 = 0.915$ (3 d); 0.867 (7 d); 0.904 (28 d)	closed-form; quick estimation
Analytical (physics-based)	Zhao et al. (Zhao et al., 2022)	Q	entrained water (from SAP), SAP-void term	Mean diff. = 5.5%p; Max diff. = 9.9%p	mechanism-informed; reference-based relative strength
ML	Hosseinzadeh et al. (Hosseinzadeh et al., 2024)	SR	dosage, particle size	RF: $R^2 = 0.86$ (MSE = 15.76); XGBoost: $R^2 = 0.88$ (MSE = 13.66); Vote: $R^2 = 0.89$ (MSE = 12.85)	data-driven; SR-oriented prediction
	This study (M2)	f_c	dosage, particle size, shape, type, absorption	$R^2 = 0.968$; MSE = 4.443; RMSE = 2.108; Accuracy = 92.70	absolute f_c; multi-dimensional SAP descriptors

f_c, compressive strength [MPa]; Q, relative compressive strength ratio (SAP mix/reference mix); SR, strength reduction [%]. SAP-void term, air/void contribution including SAP-induced voids; Adj. R^2, adjusted coefficient of determination; Vote, voting ensemble.

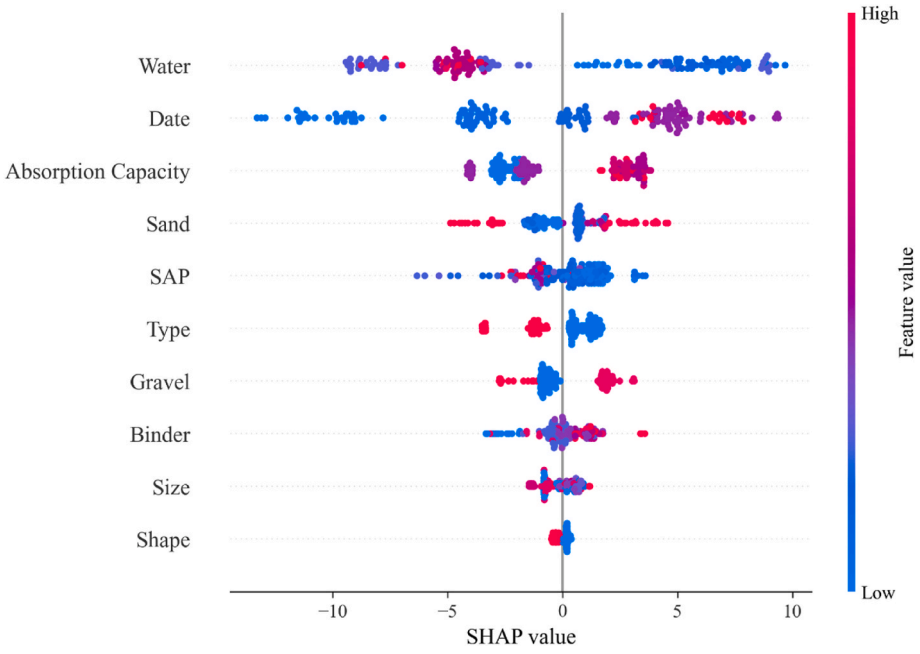


Fig. 10. SHAP summary plot for CatBoost-based M2.

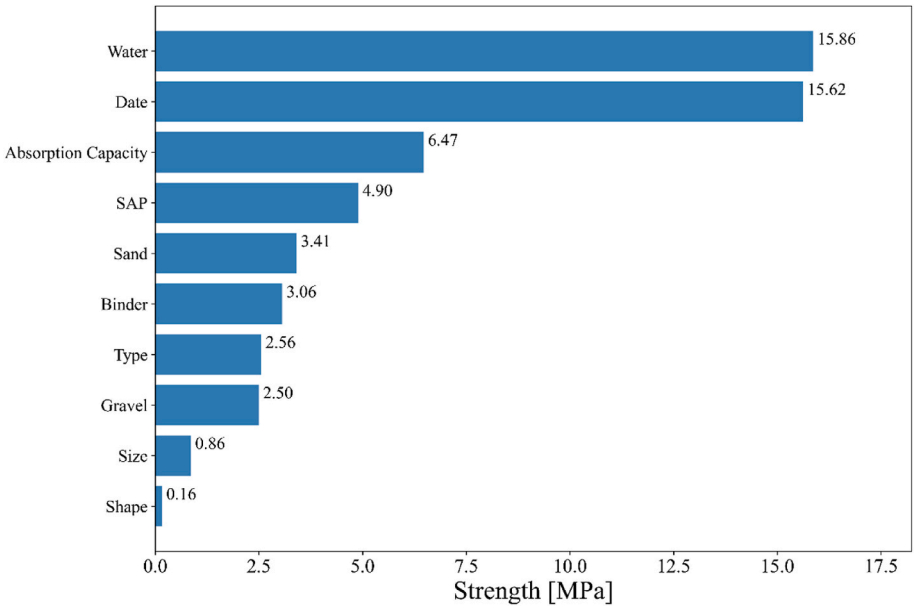


Fig. 11. PDP range (maximum-minimum) for features impacting the prediction of compressive strength using CatBoost-based M2.

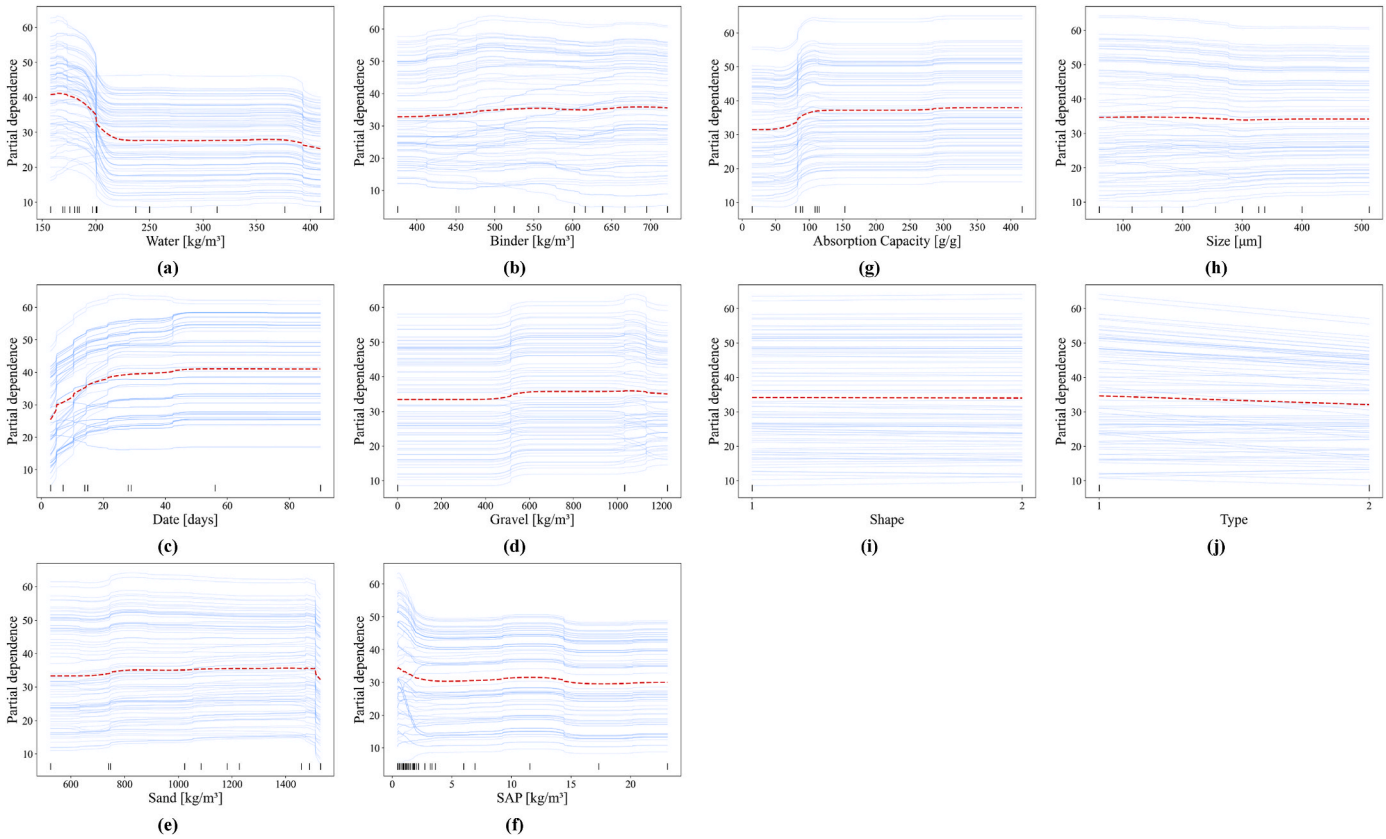


Fig. 12. Partial dependence analysis for the SAP-related variables using CatBoost-based M2: (a) *Water*, (b) *Binder*, (c) *Date*, (d) *Gravel*, (e) *Sand*, (f) *SAP*, (g) *Absorption capacity*, (h) *Size*, (i) *Shape*, and (j) *Type*. The red dashed line denotes the PDP, the light-blue curves are ICE trajectories, and the x-axis tick marks indicate the data density.

The particle size of SAPs below approximately 250 μm had a slightly negative influence on compressive strength, albeit the overall effect was limited. The absorption capacity of SAPs exhibited a sharp transition in predicted compressive strength at around 100 g/g in Fig. 12(g) and (h). These behaviors should be interpreted by jointly considering data-distribution characteristics and physical mechanisms. SAPs are incorporated primarily to supply water within the cement matrix to achieve effects such as rheology modification, mitigation of self-desiccation, and internal curing (Mechtcherine, 2016); however, a strength-related trade-off can arise because residual SAP voids formed after desorption may reduce compressive strength (Zhao et al., 2022). Accordingly, absorption capacity and particle size can be viewed as key SAP descriptors that govern the balance between the benefit of water supply and the penalty associated with residual void formation. From a data perspective, SAPs need to provide a practically sufficient water reservoir to produce a meaningful internal curing contribution; thus, too low absorption capacity may lead to limited benefits, whereas excessively high absorption can increase the void penalty after desorption. Particle size may also contribute by altering the characteristic size of SAP-induced voids; however, the PDP in Fig. 12h indicates that its overall influence is relatively limited within the studied range. Therefore, the PDP/ICE trends may partially reflect the sensitivity of strength to changes in pore size/morphology induced by SAP characteristics. Accordingly, literature-derived datasets are often concentrated within practically adopted ranges of absorption capacity (and, to a lesser extent, particle size) for internal curing applications, which can accentuate a threshold-like pattern in the PDP. From a physical standpoint, absorption capacity governs the amount of internally stored water available to sustain hydration by maintaining internal relative humidity and compensating self-desiccation (Jensen and Hansen, 2001, 2002). Once the effective stored water reaches a practically sufficient level, the internal curing contribution may become more influential, promoting continued hydration and solid-phase formation (Ding et al., 2017; Mechtcherine et al., 2014). At the same time, excessively higher absorption capacity may amplify residual void formation and pore structure changes, implying a trade-off between hydration enhancement and void-induced weakening. Accordingly, the nonlinearity observed in Fig. 12(g) and (h) may reflect the combined effects of (i) the sufficiency of internally supplied water for sustained hydration and (ii) the penalty associated with SAP-void formation. Considering the data characteristics of literature-derived datasets and the complexity of SAP–cement interactions, this behavior should be interpreted from both data-driven and mechanism-based perspectives rather than as evidence of a single deterministic threshold.

The effect of SAP particle shape on compressive strength was negligible, indicating that the model could not identify a clear pattern within the studied range. In contrast, a slight reduction in predicted compressive strength was observed using the acrylamide–acrylic acid copolymer SAP, whereas the sodium polyacrylate SAP provided higher compressive strength, suggesting that the latter could improve the mechanical performance of the resulting concrete.

4.4. Analysis using experimental data

Fig. 13 illustrates the variations in compressive strength and total porosity of cement pastes after incorporating the sodium polyacrylate SAP at dosage amounts ranging from 0 to 1.5%(bwoc; by weight of cement), while Table 10 summarizes the corresponding volumetric fractions of normal pores, SAP voids, and SAP particles quantified by using X-ray micro-CT under the same conditions. Compared with the control mix without SAPs, increasing the SAP dosage amount to 0.5, 1.0, or 1.5%(bwoc) resulted in compressive strength reductions of 18.9%,

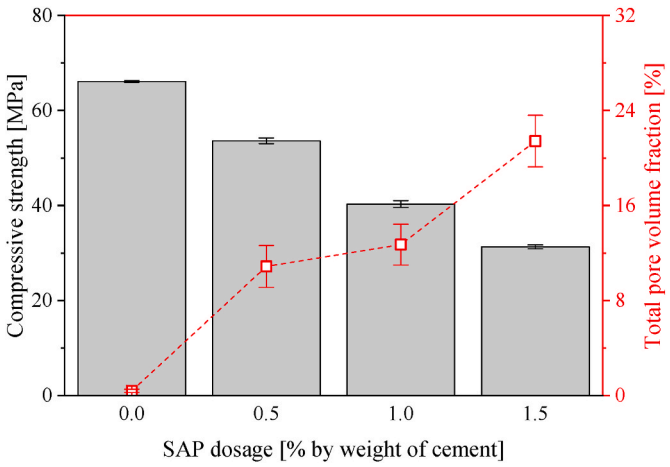


Fig. 13. Compressive strength and total pore volume fraction vs. SAP dosage amount.

Table 10
Effect of SAP dosage amount on porosity and SAP phase fractions.

SAP Dosage [%(by weight of cement)]	Normal Pores [vol%]	SAP Voids [vol%]	Total Porosity [vol%]	SAP Particles [vol%]
0	0.39 ± 0.14	—	0.39 ± 0.14	—
0.5	0.79 ± 0.06	10.08 ± 1.77	10.87 ± 1.76	1.48 ± 0.16
1.0	1.08 ± 0.13	11.63 ± 1.84	12.71 ± 1.72	1.53 ± 0.40
1.5	1.06 ± 0.11	20.36 ± 2.07	21.42 ± 2.17	3.03 ± 0.41

39.0%, and 52.6%, respectively, thus indicating a distinct downward trend with increasing SAP content. In contrast, the total porosity increased sharply with SAP dosage amount, primarily due to the predominant contribution of SAP voids rather than normal pores, as evidenced in Table 10. Furthermore, considering that the 2D segmentation process may occasionally misclassify localized SAP voids as normal pores (leading to a slight overestimation of the normal pore volume), the increase in total porosity can be more convincingly attributed to the increase in SAP voids. Nevertheless, the rate of compressive strength reduction was relatively moderate compared with the substantial increase in porosity (e.g., +10.5%p at 0.5%(bwoc), +12.3%p at 1.0% (bwoc), and +21.0%p at 1.5%(bwoc)). These observations suggest that compressive strength is significantly influenced not only by the total pore volume but also by factors such as pore size, morphology, and connectivity, as well as the degree of hydration of the solid phase (Li et al., 2018; Bu and Tian, 2016). The results indicate that the internal curing effect induced by SAPs enhanced the hydration degree and promoted the formation of additional structurally stable solid phases, which in turn partially mitigated the reduction in compressive strength despite the pronounced increase in porosity.

The water absorption and release behavior of SAPs varies depending on their chemical composition, while their particle shape differs according to the manufacturing process (Zhong et al., 2019). Table 11 summarizes the compressive strength, total porosity, mean aspect ratio, and a connectivity-related indicator of cement mortars incorporating SAPs. The connectivity indicator was derived from the X-ray micro-CT data via pore network modeling using OpenPNM (Gostick et al., 2016) and was used in this study for relative comparison among mixtures. Despite having the same SAP dosage amount, both the reduction in compressive strength and the increase in total porosity varied considerably among the cement mortars with different SAPs incorporated therein, with the total porosity differing by as much as 7.7 times. This can be attributed to differences in water absorption and release behavior: SAPs with a higher water absorption capacity tend to produce larger residual voids in the mortar after hardening. Nevertheless, the increased degree of hydration resulting from internal curing provided a compensatory effect that partially offset the loss in compressive strength. In addition, the morphology of the SAP voids was strongly dependent on the particle shape of the SAPs: irregularly shaped SAP particles increased the pore aspect ratio, whereas spherically shaped SAPs decreased it. The results also indicate an increase in pore connectivity in the SAP-incorporated mortars, with a higher connectivity value for the irregular SAP than for the spherical SAP. These observations suggest that SAP-void-induced strength reduction is not governed solely by the total porosity. Instead, pore morphology and network connectivity may also influence how SAP-induced pores interact with the surrounding matrix and the formation of continuous weak paths, thereby affecting the load-transfer network and stress distribution. Notably, although the spherical-SAP mixture exhibited a markedly higher total porosity, its pore aspect ratio was relatively low and its connectivity increase was less pronounced than that of the irregular SAP. This suggests that pore shape and connectivity can modulate the severity of SAP-void-induced strength reduction beyond the effect of pore volume alone. Figs. 14 and 15 together provide visual evidence that SAP-induced differences in pore morphology and connectivity can modify load-transfer characteristics in the cement mortar matrix.

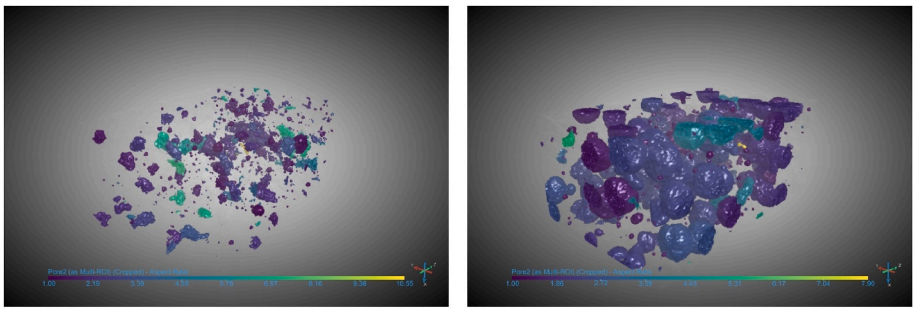
An exploratory microstructure–strength linkage analysis was additionally conducted using Spearman's rank correlation based on the X-ray micro-CT-characterized specimens. Negative monotonic association trends were observed between compressive strength and total porosity ($\rho = -0.786$) and mean aspect ratio ($\rho = -0.429$), whereas the connectivity-related indicator exhibited only a weak trend in the present dataset ($\rho = -0.143$). Because the analysis was performed on a limited combined dataset including both cement mortar and cement paste specimen groups (Table 4), these values should be interpreted as indicative trends rather than definitive relationships. Nevertheless, this exploratory microstructure–strength linkage provides complementary microstructural context to the externally validated performance of the CatBoost-based M2 summarized in Table 8, helping to inform the interpretation of the effects of SAP characteristics derived from the data-driven prediction. More definitive mechanistic validation will require a larger dataset that includes microstructure descriptors and strength measurements obtained under a consistent experimental and analysis protocol.

As discussed above, the compressive strength of SAP-incorporated cementitious materials is not merely a function of the total porosity but is also governed by the structural characteristics of the pores originating from SAP characteristics (such as particle size, shape, and type) and changes in the degree of hydration induced by internal curing. Accordingly, it can be concluded that conventional empirical equations using only total porosity as an explanatory variable are inherently

Table 11
Effect of SAP type on compressive strength and pore characteristics.

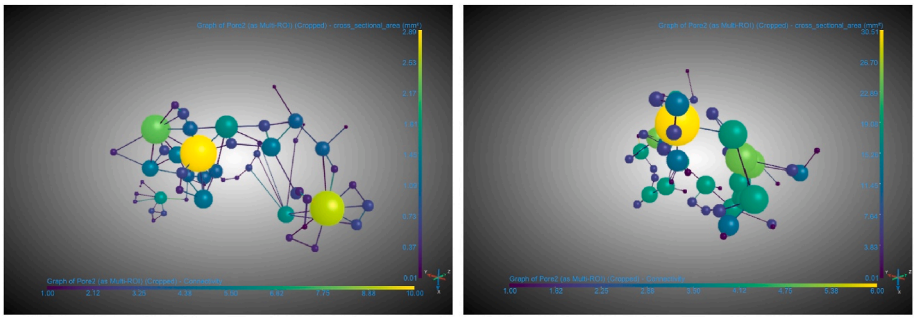
SAP Type	SAP Dosage [%(by weight of cement)]	Compressive Strength [MPa]	Total Porosity [vol%]	Pore Mean Aspect Ratio	Pore connectivity
—	—	45.44 ± 0.56	0.43 ± 0.23	1.84 ± 0.07	1.00 ± 1.00
Irregular SAP A[a]	1.0	34.16 ± 0.50	2.45 ± 0.10	2.04 ± 0.03	2.92 ± 0.30
Spherical SAP B[b]	1.0	28.25 ± 1.10	18.87 ± 0.24	1.79 ± 0.02	2.64 ± 0.12

[a] Sodium polyacrylate.
[b] Acrylamide–acrylic acid copolymer.



(a) (b)

Fig. 14. 3D X-ray micro-CT reconstructions of the pore morphology in mortar with incorporated (a) irregular sodium polyacrylate (1%(by weight of cement)) or (b) spherical acrylamide–acrylic acid copolymer (1%(by weight of cement)). The color scale denotes the pore aspect ratio.



(a) (b)

Fig. 15. Pore network models derived from X-ray micro-CT data for mortars incorporating (a) irregular sodium polyacrylate (1%(by weight of cement)) or (b) spherical acrylamide–acrylic acid copolymer (1%(by weight of cement)), used to quantify pore connectivity (e.g., vertex connectivity).

limited for accurately predicting the compressive strength of SAP-incorporated cementitious materials.

In the present study, the conventional porosity–compressive strength relationship described by the Balshin model (Eq. (12)) was refined through the introduction of an integrated index (p_{SAP}) that comprehensively accounts for the SAP characteristics. Model optimization was conducted using GA, a global optimization technique inspired by the principles of natural selection and biological evolution (Eiben and Schoenauer, 2002). Within the GA framework, each combination of variables is encoded as a chromosome, and its performance is evaluated through a fitness function. The evolutionary process iteratively produces new generations by exploiting information from the high-performing individuals. To enhance search efficiency and solution quality, an elitism strategy is employed, thereby ensuring that the best individuals are preserved across successive generations. Based on the SHAP analysis results presented in Section 4.3, p_{SAP} was constructed using the SAP-related variables identified as influential (namely SAP dosage amount, absorption capacity, and type) as input parameters. To avoid unnecessary increases in model complexity at the index-construction stage and to mitigate overfitting risk, the SAP characteristics parameter was formulated as a parsimonious linear weighted combination rather than introducing additional nonlinear terms (Peng and Nagata, 2020), thereby keeping the index simple and physically interpretable. The training data were derived from the SAP-incorporated cementitious materials dataset used for M2, where the 28-day compressive strength, SAP characteristics, and total porosity were extracted as input variables. The categorical variable representing SAP type was numerically encoded using the one-hot encoding technique. The GA parameters were set as follows: a population size of 300, a maximum of 800 generations, a crossover probability of 0.8, and a mutation probability of 0.1. Through this procedure, a GA-calibrated, Balshin-based predictive model for the compressive strength of SAP-incorporated cementitious materials was developed, as expressed in Eq. (13):

$$\sigma = \sigma_0 (1 - p)^b, \tag{12}$$

$$\sigma = \sigma_0 (1 - p_{SAP})^{0.7838}, \tag{13}$$

$$p_{SAP} = (-0.0013 + 0.0216SAP + 0.0007Absorption\ rate + 0.1000type_1 - 0.0791type_2), \tag{14}$$

where σ denotes the compressive strength of the cementitious material containing pores and σ_0 represents the compressive strength of the material without pores. In this study, to enable a strength comparison specifically with respect to SAP-induced porosity, σ_0 was substituted with the compressive strength of the SAP-free reference mixture. p denotes the total porosity, and b is a power exponent (Kearsley and Wainwright, 2002; Hoff, 1972). The sign of each coefficient in Eq. (14) indicates the direction of the corresponding SAP descriptor's contribution to p_{SAP}, in broad agreement with the SHAP derived influence patterns. Specifically, the positive coefficients for SAP dosage and absorption capacity suggest that increasing these variables tends to increase p_{SAP}, consistent with the internal-curing contribution inferred from the data. In contrast, the coefficient of the SAP type indicator variables (e.g., $type_1$ and $type_2$), defined relative to the reference category, implies that the net strength-related effect captured by p_{SAP} depends on SAP type.

To ensure a fair comparison between the two models, the empirical constant in Eq. (12) was estimated using the same training dataset that was employed to derive Eq. (13). Subsequently, the experimental data of SAP-incorporated cementitious materials were used as a validation set to calculate the RMSE and accuracy (Table 12). Eq. (13), incorporating the SAP characteristics index, exhibited a significantly lower RMSE and higher accuracy than Eq. (12), which uses only total porosity, indicating that the inclusion of SAP characteristics provides a substantial

Table 12
Performances of the models for predicting the compressive strength of SAP-incorporated cementitious materials.

Model	MSE	RMSE	MAPE based Accuracy
Balshin baseline	128.8	11.35	77.26
GA-calibrated model	48.75	6.698	83.02

improvement in predicting the compressive strength of SAP-incorporated cementitious materials—beyond a mere expansion of input variables.

The significant compressive strength prediction improvement by the proposed GA-calibrated model stems from its validation using an independent dataset that was excluded from the training range. This demonstrates that the proposed model possesses excellent generalization capability to accurately predict the compressive strength of previously unseen data. Accordingly, by incorporating the SAP characteristic index, the proposed model effectively overcomes the limitations of conventional empirical equations relying solely on total porosity (such as the Balshin baseline). Specifically, while conventional approaches require prior measurement of total porosity, the GA-calibrated model relies only on SAP characteristic variables based on the mixture design, enabling compressive strength prediction without direct porosity testing. This feature enhances the practical utility of the proposed model in both mixture design and field-oriented decision-making across a wide range of SAP-incorporated cementitious materials.

5. Practical implications, limitations and future work

This study integrates ML-based prediction with experimental validation to examine how intrinsic SAP characteristics influence the compressive strength of SAP-incorporated cementitious materials. A practical workflow for strength-oriented mix design based on the proposed model is summarized in Fig. 16. In a typical application, the designer first specifies a target compressive strength at the intended age ($f_{c.Target}$; 28 days is recommended in this study because the compiled database is most densely populated at 28 days) and then defines a feasible design window for mixture variables (binder, aggregates, and water) together with SAP descriptors (dosage, particle size, shape, type, and absorption capacity). After processing the inputs in a manner consistent with the definitions used in the M2 database, the CatBoost-based M2 is applied to obtain the predicted strength ($f_{c.Pr\ edict}$), and candidate mixes can be screened by iteratively adjusting controllable inputs to meet the target. As confirmed in this study, water content, absorption capacity, and SAP type exert strong influence on predictions; thus, these variables should be prioritized during the adjustment process. Accordingly, water should reflect the specified mixing water content, while absorption capacity and SAP type should be provided based on reliable measurements and dataset-consistent classification criteria rather than assumed estimates. It should also be noted that the current M2 was trained predominantly on mortar/concrete data and includes limited paste-only cases; therefore, predictions for cement paste mixtures should be interpreted cautiously at this stage. Compared with trial-and-error mix adjustment based primarily on experience, this prediction-based screening procedure enables rapid estimation of strength levels and efficient narrowing of the design space. Moreover, following the standardized input processing and implementation steps in Fig. 16 simplifies model use in practice, allowing the model to serve as a first-pass screening tool for candidate mixes. The preprocessed dataset, the CatBoost-based M2 model training and SHAP-analysis scripts are

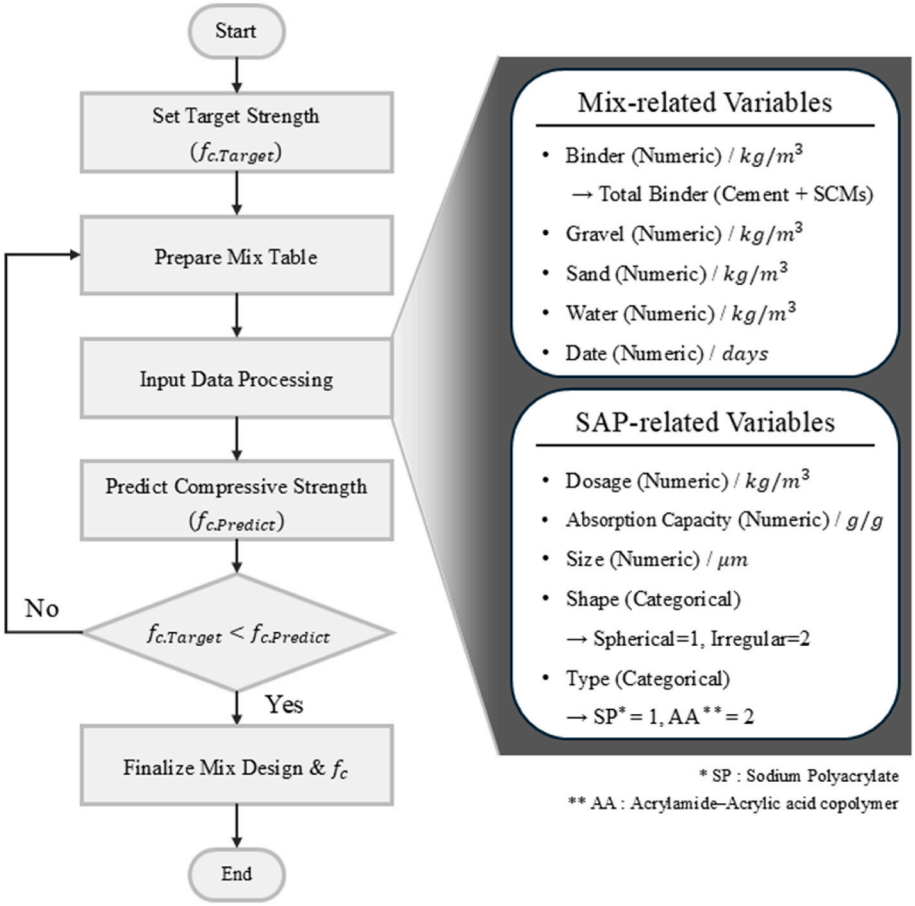


Fig. 16. Workflow for implementing the CatBoost-based M2 model for mix design selection using mixed-type inputs.

available at https://doi.org/10.5281/zenodo.18753732.

In this study, ML models were developed to predict the compressive strength of SAP-incorporated cementitious materials, and the relationships between SAP descriptors and strength were examined using model-interpretation analyses together with complementary experiments, including compressive strength testing and X-ray micro-CT-based pore structure analysis. As an example of practical use of the developed model for mix design, a strength-oriented workflow is also presented. Nevertheless, several limitations remain that may restrict the generalization and practical implementation of the proposed findings, as follows.

(i) ***Data volume and representativeness.*** Compared with plain cementitious materials, the dataset for SAP-incorporated cementitious materials is limited in size because the available data have been primarily collected from published experimental studies. To ensure the robustness of the quantitative results, the dataset should be continuously refined, expanded, and updated by incorporating new data as further experimental research on SAP-incorporated cementitious materials becomes available. In particular, improving coverage for underrepresented categorical SAP levels (e.g., specific types/shapes) and paste-only systems is an important next step to broaden applicability. In addition, because compressive strength exhibits inherent experimental scatter, providing explicit prediction uncertainty would require either replicate-level data or dedicated uncertainty-quantification procedures. Therefore, uncertainty-aware prediction is identified as a future extension.

(ii) ***Variable interdependence and factor disentanglement.*** Intercorrelations among the input variables can lead to fluctuations in the predicted output due to mutual interactions. However, because of the limited sample size, it is difficult to implement controlled factor arrangements or sufficient covariate adjustments, which restricts the ability to isolate and accurately estimate the independent effects of each variable. As the dataset is expanded in future studies, more sophisticated statistical designs and preprocessing procedures, including factor separation and interaction analysis, will be possible. Future work can also leverage expanded datasets to perform more reliable interaction quantification and subgroup analyses across SAP systems.

(iii) ***Heterogeneity of experimental and evaluation protocols.*** Variations in the SAP incorporation methods and testing procedures among the different studies might have introduced bias into the reported results. Consequently, it is recommended to select data obtained under identical or comparable experimental protocols, apply preprocessing corrections to account for testing method effects, and/or establish new datasets generated under a unified experimental framework. Future datasets should systematically include protocol-related metadata (e.g., curing regime, specimen geometry, and test method) to enable their explicit treatment during preprocessing/modeling and thereby improve prediction accuracy and generalizability.

(iv) ***Limitations in mechanism interpretation due to restricted experimental methods.*** This study integrated feature importance analysis with experimental observations to examine the effects of each SAP characteristic. However, the diversity and resolution of applicable experimental techniques were limited, thus making it difficult to elucidate the detailed mechanisms associated with each factor. As a result, while the overall trends and effect directions were identified, the quantitative estimation accuracy could still be improved. A concrete next step is to strengthen the microstructure–macro-property linkage by incorporating experimentally quantified pore-structure descriptors (e.g., porosity, aspect ratio, and connectivity) into modeling and validation under a consistent experimental and analysis protocol.

Nevertheless, the outcomes from this study confirm that predicting the compressive strength of SAP-incorporated cementitious materials is more complex than for conventional cementitious materials due to the intrinsic characteristics of SAPs. By applying appropriate ML techniques and linking data-driven analyses with X-ray micro-CT indicators, the influence of SAP characteristics on compressive strength was systematically investigated. The findings of this study can serve as a foundational reference for advancing the understanding of SAP-incorporated cementitious materials, constructing standardized databases, guiding future efforts toward practical applications, and providing more accurate compressive strength prediction frameworks.

6. Conclusions

This study developed ML-based models to predict the compressive strength of cementitious materials incorporating SAPs, in which SAP characteristics (dosage amount, particle size, absorption capacity, particle shape, and type) were explicitly included as input variables. In addition, the model interpretations were complemented by experimental investigations using X-ray micro-CT to examine the contributions of SAP characteristics to compressive strength. The key findings can be summarized as follows.

1. M2 was trained using five ML techniques (DNN, KRR, RF, XGBoost, and CatBoost), and their predictive performances were evaluated based on R^2, MSE, RMSE, and MAPE based accuracy. Among them, CatBoost-based M2 demonstrated the best performance (R^2 of 0.9680, MSE of 4.443, RMSE of 2.108, and accuracy of 92.70%), followed by XGBoost and RF. This superior performance can be attributed to CatBoost's ability to effectively capture nonlinearities and feature interactions, as well as its robust handling of categorical SAP features through ordered boosting and target statistics, which together enhanced prediction reliability even under the limited sample size and moderate heterogeneity of the present dataset.
2. According to the SHAP and PDP with ICE analyses, the most influential input variables affecting compressive strength were the water content and curing age, which exhibited negative and positive effects, respectively. Among the SAP characteristics, the order of importance was absorption capacity, dosage amount, type, particle size, and shape. The PDP results reveal that the predicted compressive strength varied by 6.47, 4.90, and 2.56 MPa with respect to these three SAP characteristics, respectively. In contrast, the effects of particle size and shape were relatively minor within the observation range of this study, albeit a negative influence of a smaller particle size ($<$250 μm) on compressive strength was observed.
3. The results from X-ray micro-CT measurements of the pore characteristics and compressive strength testing indicate that compressive strength is governed not only by the total porosity but also by the pore distribution and morphology, as well as the hydration degree. The influence of these factors was further amplified by the characteristics of SAPs, leading to increased prediction complexity compared to that for plain cementitious materials. When the conventional porosity–strength empirical model was compared with the GA-calibrated equation incorporating the SAP characteristics, the latter demonstrated a significant performance improvement, as evidenced by lower RMSE and higher accuracy values. These results indicate that incorporating SAP characteristics into predictive models is effective for improving the accuracy of compressive strength prediction for SAP-incorporated cementitious materials.

CRediT authorship contribution statement

Dohyeong Kim: Conceptualization, Data curation, Investigation, Methodology, Software, Visualization, Writing – original draft, Writing – review & editing. **Sangwoo Oh:** Conceptualization, Data curation, Formal analysis, Software, Visualization, Writing – original draft,

Writing – review & editing. **Seongcheol Choi:** Validation. **Geuntae Hong:** Conceptualization, Funding acquisition, Project administration, Resources, Supervision, Writing – review & editing.

Declaration of competing interest

The authors declare the following financial interests/personal relationships which may be considered as potential competing interests: Geuntae Hong reports financial support was provided by National Research Foundation of Korea. If there are other authors, they declare that they have no known competing financial interests or personal relationships that could have appeared to influence the work reported in this paper.

Acknowledgments

This work was supported by the National Research Foundation of Korea (NRF) grant funded by the Korea government (MSIT) (No. RS-2023-00211399); the National Research Foundation of Korea (NRF) grant funded by the Korea government (MSIT) (No. RS-2025-02216342).

Data availability

Data will be made available on request.

References

Aby, A.E., Salaji, S., Anilkumar, K.K., Rajan, T., 2025. Classification of acute myeloid leukemia by pre-trained deep neural networks: a comparison with different activation functions. Med. Eng. Phys. 135, 104277. https://doi.org/10.1016/j.medengphy.2024.104277.

Aceña, V., de Diego, I.M., Fernández, R.R., Moguerza, J.M., 2022. Minimally overfitted learners: a general framework for ensemble learning. Knowl.-Based Syst. 254, 109669. https://doi.org/10.1016/j.knosys.2022.109669.

Adesina, A., Zhang, J., 2024. Impact of concrete structures durability on its sustainability and climate resiliency. Sustain. Times 3, 100025. https://doi.org/10.1016/j.nxsust.2024.100025.

Al-Gahtani, A.S., 2010. Effect of curing methods on the properties of plain and blended cement concretes. Constr. Build. Mater. 24 (3), 308–314. https://doi.org/10.1016/j.conbuildmat.2009.08.036.

Al-Jamimi, H.A., Al-Kutti, W.A., Alwahaishi, S., Alotaibi, K.S., 2022. Prediction of compressive strength in plain and blended cement concretes using a hybrid artificial intelligence model. Case Stud. Constr. Mater. 17, e01238. https://doi.org/10.1016/j.cscm.2022.e01238.

Al-Shawafi, A., Zhu, H., Haruna, S.I., Ibrahim, Y.E., Yang, J., Borito, S.M., 2024. Experimental study of a superabsorbent polymer hydrogel in an alkali environment and its effects on the mechanical and shrinkage properties of cement mortars. Polymers 16 (8), 1158. https://doi.org/10.3390/polym16081158.

Ali, S., Akhlaq, F., Imran, A.S., Kastrati, Z., Daudpota, S.M., Moosa, M., 2023. The enlightening role of explainable artificial intelligence in medical & healthcare domains: a systematic literature review. Comput. Biol. Med. 166, 107555. https://doi.org/10.1016/j.compbiomed.2023.107555.

Apley, D.W., Zhu, J., 2020. Visualizing the effects of predictor variables in black box supervised learning models. J. R. Stat. Soc. Ser. B: Stat. Methodol. 82 (4), 1059–1086. https://doi.org/10.1111/rssb.12377.

Arckarapunyathorn, W., Markpiban, P., Sahamitmongkol, R., 2025. Effect of superabsorbent polymer size on strength and shrinkage in concrete mixtures. Polymers 17 (14), 1942. https://doi.org/10.3390/polym17141942.

Ascari, E., Cerchiai, M., Fredianelli, L., Melluso, D., Rampino, F., Licitra, G., 2023. Decision trees and labeling of low noise pavements as support for noise action plans. Environ. Pollut. 337, 122487. https://doi.org/10.1016/j.envpol.2023.122487.

ASTM International, 2020. Standard Test Method for Flow of Hydraulic Cement Mortar. ASTM C1437-20. https://doi.org/10.1520/C1437-20.

ASTM International, 2024. Standard Specification for Portland Cement. ASTM C150/C150M-24. https://doi.org/10.1520/C0150_C0150M-24.

Balshin, M.Y., 1949. Dependence of mechanical properties of metal powders on porosity and limiting properties of metal–ceramic materials. Dokl. Akad. Nauk. USSR 67, 831–834.

Barkhordari, M.S., Ghavaminejad, S., Tehranizadeh, M., 2024. Predicting autogenous shrinkage of concrete including superabsorbent polymers and other cementitious ingredients using convolution-based algorithms. Period. Polytech. Civ. Eng. 68 (4), 1098–1121. https://doi.org/10.3311/PPci.23568.

Belgiu, M., Drăguţ, L., 2016. Random forest in remote sensing: a review of applications and future directions. ISPRS J. Photogrammetry Remote Sens. 114, 24–31. https://doi.org/10.1016/j.isprsjprs.2016.01.011.

Beushausen, H., Gillmer, M., Alexander, M., 2014. The influence of superabsorbent polymers on strength and durability properties of blended cement mortars. Cem. Concr. Compos. 52, 73–80. https://doi.org/10.1016/j.cemconcomp.2014.03.008.

Bühlmann, P., Yu, B., 2003. Boosting with the L_2 loss: regression and classification. J. Am. Stat. Assoc. 98 (462), 324–339. https://doi.org/10.1198/016214503000125.

Breiman, L., 2001. Random forests. Mach. Learn. 45, 5–32. https://doi.org/10.1023/A:1010933404324.

Bu, J., Tian, Z., 2016. Relationship between pore structure and compressive strength of concrete: experiments and statistical modeling. Sādhanā 41, 337–344. https://doi.org/10.1007/s12046-016-0468-9.

C, P., Marques, F., 2022. Confidence intervals for the random forest generalization error. Pattern Recognit. Lett. 158, 171–175. https://doi.org/10.1016/j.patrec.2022.04.031.

Cavaleri, L., Barkhordari, M.S., Repapis, C.C., Armaghani, D.J., Ulrikh, D.V., Asteris, P.G., 2022. Convolution-based ensemble learning algorithms to estimate the bond strength of the corroded reinforced concrete. Constr. Build. Mater. 359, 129504. https://doi.org/10.1016/j.conbuildmat.2022.129504.

Cervantes, J., Lamont, F.G., Mazahua, L.R., Lopez, A., 2020. A comprehensive survey on support vector machine classification: applications, challenges and trends. Neurocomputing 408, 189–215. https://doi.org/10.1016/j.neucom.2019.10.118.

Chaabene, W.B., Flah, M., Nehdi, M.L., 2020. Machine learning prediction of mechanical properties of concrete: critical review. Constr. Build. Mater. 260, 119889. https://doi.org/10.1016/j.conbuildmat.2020.119889.

Chelgani, S.C., Nasiri, H., Tohry, A., Heidari, H.R., 2023. Modeling industrial hydrocyclone operational variables by SHAP-CatBoost - a "conscious lab" approach. Powder Technol. 420, 118416. https://doi.org/10.1016/j.powtec.2023.118416.

Chen, D., He, Q., Wang, X., 2010. FRSVMs: Fuzzy rough set based support vector machines. Fuzzy Set Syst. 161 (4), 596–607. https://doi.org/10.1016/j.fss.2009.04.007.

Chen, F., Liu, H., Qiao, J., Gou, H., Guan, X., 2025. Effect of superabsorbent polymer (SAP) on the early hydration and macro-properties of cement paste: a novel perspective based on water migration. Constr. Build. Mater. 472, 140792. https://doi.org/10.1016/j.conbuildmat.2025.140792.

Chen, T., Guestrin, C., 2016. XGBoost: a scalable tree boosting system. In: Krishnapuram, B., Shah, M., Rastogi, R., Shen, D., Aggarwal, C., Smola, A. (Eds.), Proceedings of the 22nd ACM SIGKDD International Conference on Knowledge Discovery and Data Mining (KDD '16). Association for Computing Machinery, New York, pp. 785–794.

Chen, Y., Zhang, Y., Pang, B., Wang, D., Liu, Z., Liu, G., 2022. Steel fiber orientational distribution and effects on 3D printed concrete with coarse aggregate. Mater. Struct. 55, 100. https://doi.org/10.1617/s11527-022-01943-7.

Chindasiriphan, P., Yokota, H., Pimpakan, P., 2020. Effect of fly ash and superabsorbent polymer on concrete self-healing ability. Constr. Build. Mater. 233, 116975. https://doi.org/10.1016/j.conbuildmat.2019.116975.

Cánovas-García, F., Alonso-Sarría, F., Gomariz-Castillo, F., Oñate-Valdivieso, F., 2017. Modification of the random forest algorithm to avoid statistical dependence problems when classifying remote sensing imagery. Comput. Geosci. 103, 1–11. https://doi.org/10.1016/j.cageo.2017.02.012.

Cortes, C., Vapnik, V., 1995. Support-vector networks. Mach. Learn. 20, 273–297. https://doi.org/10.1007/BF00994018.

Dang, J., Zhao, J., Du, Z., 2017. Effect of superabsorbent polymer on the properties of concrete. Polymers 9 (12), 672. https://doi.org/10.3390/polym9120672.

Ding, H., Zhang, L., Zhang, P., 2017. Factors influencing strength of Super Absorbent Polymer (SAP) concrete. Trans. Tianjin Univ. 23, 245–257. https://doi.org/10.1007/s12209-017-0049-y.

Douak, F., Melgani, F., Benoudjit, N., 2013. Kernel ridge regression with active learning for wind speed prediction. Appl. Energy 103, 328–340. https://doi.org/10.1016/j.apenergy.2012.09.055.

Eiben, A.E., Schoenauer, M., 2002. Evolutionary computing. Inf. Process. Lett. 82 (1), 1–6. https://doi.org/10.1016/S0020-0190(02)00204-1.

European Committee for Standardization (CEN), 2021. Concrete — Specification, Performance, Production and Conformity, EN 206:2013+A2:2021.

Feng, D.-C., Liu, Z.-T., Wang, X.-D., Chen, Y., Chang, J.-Q., Wei, D.-F., Jiang, Z.-M., 2020. Machine learning-based compressive strength prediction for concrete: an adaptive boosting approach. Constr. Build. Mater. 230, 117000. https://doi.org/10.1016/j.conbuildmat.2019.117000.

Freund, Y., Schapire, R.E., 1997. A decision-theoretic generalization of On-Line learning and an application to boosting. J. Comput. Syst. Sci. 55 (1), 119–139. https://doi.org/10.1006/jcss.1997.1504.

Friedman, J.H., 2001. Greedy function approximation: a gradient boosting machine. Ann. Stat. 29 (5), 1189–1232. https://doi.org/10.1214/aos/1013203451.

Friedman, J.H., 2002. Stochastic gradient boosting. Comput. Stat. Data Anal. 38 (4), 367–378. https://doi.org/10.1016/S0167-9473(01)00065-2.

Friedman, J., Hastie, T., Tibshirani, R., 2000. Additive logistic regression: a statistical view of boosting. Ann. Stat. 28 (2), 337–407. https://doi.org/10.1214/aos/1016218223.

Goldstein, A., Kapelner, A., Bleich, J., Pitkin, E., 2015. Peeking inside the black box: visualizing statistical learning with plots of individual conditional expectation. J. Comput. Graph Stat. 24 (1), 44–65. https://doi.org/10.1080/10618600.2014.907095.

Gostick, J., Aghighi, M., Hinebaugh, J., Tranter, T., Hoeh, M.A., Day, H., Spellacy, B., Sharqawy, M.H., Bazylak, A., Burns, A., Lehnert, W., Putz, A., 2016. OpenPNM: a pore network modeling package. Comput. Sci. Eng. 18 (4), 60–74. https://doi.org/10.1109/MCSE.2016.49.

Hapfelmeier, A., Hornung, R., Haller, B., 2023. Efficient permutation testing of variable importance measures by the example of random forests. Comput. Stat. Data Anal. 181, 107689. https://doi.org/10.1016/j.csda.2022.107689.
Hastie, T., Tibshirani, R., Friedman, J., 2009. The Elements of Statistical Learning: Data Mining, Inference, and Prediction, second ed. Springer, New York.
He, H., Garcia, E.A., 2009. Learning from imbalanced data. IEEE Trans. Knowl. Data Eng. 21 (9), 1263–1284. https://doi.org/10.1109/TKDE.2008.239.
Hilloulin, B., Tran, V.Q., 2022. Using machine learning techniques for predicting autogenous shrinkage of concrete incorporating superabsorbent polymers and supplementary cementitious materials. J. Build. Eng. 49, 104086. https://doi.org/10.1016/j.jobe.2022.104086.
Hoff, G.C., 1972. Porosity-strength considerations for cellular concrete. Cement Concr. Res. 2 (1), 91–100. https://doi.org/10.1016/0008-8846(72)90026-9.
Hong, G., Kim, J., Song, C., Yeon, J.H., Choi, S., 2024. Effect of internal curing by superabsorbent polymers on the densification and microstructural development of cementitious materials exposed to different environmental conditions. Constr. Build. Mater. 411, 134778. https://doi.org/10.1016/j.conbuildmat.2023.134778.
Hong, G., Song, C., Park, J., Choi, S., 2019. Hysteretic behavior of rapid self-sealing of cracks in cementitious materials incorporating superabsorbent polymers. Constr. Build. Mater. 195, 187–197. https://doi.org/10.1016/j.conbuildmat.2018.11.075.
Hosseinzadeh, M., Mousavi, S.S., Dehestani, M., 2024. An ensemble learning-based prediction model for the compressive strength degradation of concrete containing superabsorbent polymers (SAP). Sci. Rep. 14, 18535. https://doi.org/10.1038/s41598-024-68276-z.
Hu, X., Kang, S., Xue, S., Zhu, S., 2025. Explainable robo-advisor: an online learning framework for new investors without trading records. Neurocomputing 624, 129463. https://doi.org/10.1016/j.neucom.2025.129463.
Huang, F., Shangguan, W., Li, Q., Li, L., Zhang, Y., 2023. Beyond prediction: an integrated post-hoc approach to interpret complex model in hydrometeorology. Environ. Model. Software 167, 105762. https://doi.org/10.1016/j.envsoft.2023.105762.
Hussain, S.F., 2019. A novel robust kernel for classifying high-dimensional data using support vector machines. Expert Syst. Appl. 131, 116–131. https://doi.org/10.1016/j.eswa.2019.04.037.
International Organization for Standardization (ISO), 2009. Cement – Test Methods –Determination of Strength. ISO 679.
Jabeur, S.B., Gharib, C., Wali, S.M., Arfi, W.B., 2021. CatBoost model and artificial intelligence techniques for corporate failure prediction. Technol. Forecast. Soc. Change 166, 120658. https://doi.org/10.1016/j.techfore.2021.120658.
Jensen, O.M., Hansen, P.F., 2001. Water-entrained cement-based materials: I. Principles and theoretical background. Cement Concr. Res. 31 (4), 647–654. https://doi.org/10.1016/S0008-8846(01)00463-X.
Jensen, O.M., Hansen, P.F., 2002. Water-entrained cement-based materials: II. Experimental observations. Cement Concr. Res. 32 (6), 973–978. https://doi.org/10.1016/S0008-8846(02)00737-8.
Kearsley, E.P., Wainwright, P.J., 2002. The effect of porosity on the strength of foamed concrete. Cement Concr. Res. 32 (2), 233–239. https://doi.org/10.1016/S0008-8846(01)00665-2.
Khan, S.H., Hayat, M., Porikli, F., 2019. Regularization of deep neural networks with spectral dropout. Neural Netw. 110, 82–90. https://doi.org/10.1016/j.neunet.2018.09.009.
Kiliçarslan, S., Celik, M., 2021. "RSigELU: a nonlinear activation function for deep neural networks. Expert Syst. Appl. 174, 114805. https://doi.org/10.1016/j.eswa.2021.114805.
Kilimci, Z.H., Akyuz, A.O., Uysal, M., Akyokus, S., Uysal, M.O., Bulbul, B.A., Ekmis, M.A., 2019. An improved demand forecasting model using deep learning approach and proposed decision integration strategy for supply chain. Complex 2019, 9067367. https://doi.org/10.1155/2019/9067367.
Krawczyk, B., 2016. Learning from imbalanced data: open challenges and future directions. Prog. Artif. Intell. 5, 221–232. https://doi.org/10.1007/s13748-016-0094-0.
Kumar, R., Althaqafi, E., Patro, S.G.K., Simic, V., Babbar, A., Pamucar, D., Singh, S.K., Verma, A., 2024. Machine and deep learning methods for concrete strength prediction: a bibliometric and content analysis review of research trends and future directions. Appl. Soft Comput. 164, 111956. https://doi.org/10.1016/j.asoc.2024.111956.
Lauriola, I., Gallicchio, C., Aiolli, F., 2020. Enhancing deep neural networks via multiple kernel learning. Pattern Recogn. 101, 107194. https://doi.org/10.1016/j.patcog.2020.107194.
Li, D., Li, Z., Lv, C., Zhang, G., Yin, Y., 2018. A predictive model of the effective tensile and compressive strengths of concrete considering porosity and pore size. Constr. Build. Mater. 170, 520–526. https://doi.org/10.1016/j.conbuildmat.2018.03.028.
Li, T., Li, E., Duan, H., Chu, Z., Wang, J., Chen, W., 2024. Artificial neural network models for metal-ferroelectric-insulator-semiconductor ferroelectric tunnel junction memristor. Microelectron. J. 144, 106083. https://doi.org/10.1016/j.mejo.2023.106083.
Li, Z., Tian, L., Yan, X., 2023. A multi-objective optimization based deep feature multi-subspace partitioning method for process monitoring. Expert Syst. Appl. 225, 120097. https://doi.org/10.1016/j.eswa.2023.120097.
Liang, X., Xu, J., 2021. Biased ReLU neural networks. Neurocomputing 423, 71–79. https://doi.org/10.1016/j.neucom.2020.09.050.
Liu, Y., Liang, R., Zhang, C., 2024. The application of machine learning algorithms for predicting length of stay before and during the COVID-19 pandemic: evidence from Wuhan-area hospitals. Front. Digit. Health 6, 1506071. https://doi.org/10.3389/fdgth.2024.1506071.
Lorenzoni, R., Curosu, I., Paciornik, S., Mechtcherine, V., Oppermann, M., Silva, F., 2020. Semantic segmentation of the micro-structure of strain-hardening cement-based composites (SHCC) by applying deep learning on micro-computed tomography scans. Cem. Concr. Compos. 108, 103551. https://doi.org/10.1016/j.cemconcomp.2020.103551.
Lundberg, S.M., Lee, S.-I., 2017. A unified approach to interpreting model predictions. In: Guyon, I., Luxburg, U.V., Bengio, S., Wallach, H., Fergus, R., Vishwanathan, S., Garnett, R. (Eds.), Advances in Neural Information Processing Systems 30. Curran Associates, Inc., CA, pp. 1–10.
Lyu, Z., Shen, A., Meng, W., 2021. Properties, mechanism, and optimization of superabsorbent polymers and basalt fibers modified cementitious composite. Constr. Build. Mater. 276, 122212. https://doi.org/10.1016/j.conbuildmat.2020.122212.
Maier, H.R., Galelli, S., Razavi, S., Castelletti, A., Rizzoli, A., Athanasiadis, I.N., Marrè, M.S., Acutis, M., Wu, W., Humphrey, G.B., 2023. Exploding the myths: an introduction to artificial neural networks for prediction and forecasting. Environ. Model. Software 167, 105776. https://doi.org/10.1016/j.envsoft.2023.105776.
Mechtcherine, V., 2016. Use of superabsorbent polymers (SAP) as concrete additive. RILEM Tech. Lett. 1, 81–87. https://doi.org/10.21809/rilemtechlett.2016.18.
Mechtcherine, V., Gorges, M., Schroefl, C., Assmann, A., Brameshuber, W., Ribeiro, A.B., Cusson, D., Custódio, J., da Silva, E.F., Ichimiya, K., Igarashi, S.-I., Klemm, A., Kovler, K., Lopes, A.N. de M., Lura, P., Nguyen, V.T., Reinhardt, H.-W., Filho, R.D.T., Weiss, J., Wyrzykowski, M., Ye, G., Zhutovsky, S., 2014. Effect of internal curing by using superabsorbent polymers (SAP) on autogenous shrinkage and other properties of a high-performance fine-grained concrete: results of a RILEM round-robin test. Mater. Struct. 47, 541–562. https://doi.org/10.1617/s11527-013-0078-5.
Molnar, C., König, G., Herbinger, J., Freiesleben, T., Dandl, S., Scholbeck, C.A., Casalicchio, G., Wentrup, M.G., Bischl, B., 2022. General pitfalls of model-agnostic interpretation methods for machine learning models. In: Holzinger, A., Goebel, R., Fong, R., Moon, T., Müller, K.-R., Samek, W. (Eds.), Xxai – Beyond Explainable AI. Springer International Publishing, Cham, pp. 39–68.
Nakayama, Y., Yata, K., Aoshima, M., 2017. Support vector machine and its bias correction in high-dimension, low-sample-size settings. J. Stat. Plann. Inference 191, 88–100. https://doi.org/10.1016/j.jspi.2017.05.005.
Narayanan, S., 2024. Effect of size and shape of test specimen on compressive strength of concrete. Concr. Int. 46 (1), 45–51. https://doi.org/10.14359/51740319.
Neubauer, A., Brandt, S., Kriegel, M., 2025. Explainable multi-step heating load forecasting: using SHAP values and temporal attention mechanisms for enhanced interpretability. Energy AI 20, 100480. https://doi.org/10.1016/j.egyai.2025.100480.
Nguyen, H., Vu, T., Vo, T.P., Thai, H.-T., 2021. Efficient machine learning models for prediction of concrete strengths. Constr. Build. Mater. 266, 120950. https://doi.org/10.1016/j.conbuildmat.2020.120950.
Ni, B., Rahman, M.Z., Guo, S., Zhu, D., 2025. A review on properties and multi-objective performance predictions of concrete based on machine learning models. Mater. Today Commun. 44, 112017. https://doi.org/10.1016/j.mtcomm.2025.112017.
Nithurshan, M., Elakneswaran, Y., 2023. A systematic review and assessment of concrete strength prediction models. Case Stud. Constr. Mater. 18, e01830. https://doi.org/10.1016/j.cscm.2023.e01830.
Patil, A.D., Ravande, K., Jadhav, S., Junead, M., 2023. Effect of superabsorbent polymer and slag cement on concrete properties. Mater. Today Proc. https://doi.org/10.1016/j.matpr.2023.06.037.
Peng, Y., Nagata, M.H., 2020. An empirical overview of nonlinearity and overfitting in machine learning using COVID-19 data. Chaos Solitons Fractals 139, 110055. https://doi.org/10.1016/j.chaos.2020.110055.
Petersen, M.L., Molinaro, A.M., Sinisi, S.E., van der Laan, M.J., 2007. Cross-validated bagged learning. J. Multivariate Anal. 98 (9), 1693–1704. https://doi.org/10.1016/j.jmva.2007.07.004.
Prasad, B.K.R., Eskandari, H., Reddy, B.V.V., 2009. Prediction of compressive strength of SCC and HPC with high volume fly ash using ANN. Constr. Build. Mater. 23 (1), 117–128. https://doi.org/10.1016/j.conbuildmat.2008.01.014.
Pressmair, N., Brosch, F., Hammerl, M., Kromoser, B., 2022. Non-linear material modelling strategy for conventional and high-performance concrete assisted by testing. Cement Concr. Res. 161, 106933. https://doi.org/10.1016/j.cemconres.2022.106933.
Prokhorenkova, L., Gusev, G., Vorobev, A., Dorogush, A.V., Gulin, A., 2018. CatBoost: unbiased boosting with categorical features. In: Bengio, S., Wallach, H., Larochelle, H., Grauman, K., C.-Bianchi, N., Garnett, R. (Eds.), Advances in Neural Information Processing Systems 31. Curran Associates, Inc., Montreal, pp. 1–11.
Qureshi, H.J., Saleem, M.U., Javed, M.F., Fuhaid, A.F.A., Ahmad, J., Amin, M.N., Khan, K., Aslam, F., Arifuzzaman, M., 2022. Prediction of autogenous shrinkage of concrete incorporating super absorbent polymer and waste materials through individual and ensemble machine learning approaches. Materials 15 (21), 7412. https://doi.org/10.3390/ma15217412.
Ran, L., Wang, Z., Yang, B., Margavi, A.A., Alshahrani, N., 2024. Development of novel computational models based on artificial intelligence technique to predict the viscosity of ionic liquids-water mixtures. Case Stud. Therm. Eng. 54, 104076. https://doi.org/10.1016/j.csite.2024.104076.
Retzlaff, C.O., Angerschmid, A., Saranti, A., Schneeberger, D., Röttger, R., Müller, H., Holzinger, A., 2024. Post-hoc vs ante-hoc explanations: xAI design guidelines for data scientists. Cogn. Syst. Res. 86, 101243. https://doi.org/10.1016/j.cogsys.2024.101243.
Rosa, Á.D.L., Ruiz, G., 2025. A new approach to the study of the size and the geometry effect on compressive strength in concrete. Results Eng. 25, 104261. https://doi.org/10.1016/j.rineng.2025.104261.

Schröfl, C., Erk, K.A., Siriwatwechakul, W., Wyrzykowski, M., Snoeck, D., 2022. Recent progress in superabsorbent polymers for concrete. Cement Concr. Res. 151, 106648. https://doi.org/10.1016/j.cemconres.2021.106648.

Seki, Y., Shibayama, A., Nishiyama, M., Kikuchi, M., 2024. Machine learning models for predicting the compressive strengths of ordinary Portland cement concrete and alkali-activated materials. Sustain. Mater. Technol. 42, e01191. https://doi.org/10.1016/j.susmat.2024.e01191.

Sexton, J., Laake, P., 2009. Standard errors for bagged and random forest estimators. Comput. Stat. Data Anal. 53 (3), 801–811. https://doi.org/10.1016/j.csda.2008.08.007.

Shamsabadi, E.A., Roshan, N., Hadigheh, S.A., Nehdi, M.L., Khodabakhshian, A., Ghalehnovi, M., 2022. Machine learning-based compressive strength modelling of concrete incorporating waste marble powder. Constr. Build. Mater. 324, 126592. https://doi.org/10.1016/j.conbuildmat.2022.126592.

Shwartz-Ziv, R., Armon, A., 2022. Tabular data: deep learning is not all you need. Inf. Fusion 81, 84–90. https://doi.org/10.1016/j.inffus.2021.11.011.

Singh, N., Singh, A., Ankur, N., Kumar, P., Kumar, M., Singh, T., 2022. Reviewing the properties of recycled concrete aggregates and iron slag in concrete. J. Build. Eng. 60, 105150. https://doi.org/10.1016/j.jobe.2022.105150.

Song, J., 2015. Bias corrections for random forest in regression using residual rotation. J. Korean Surg. Soc. 44, 321–326. https://doi.org/10.1016/j.jkss.2015.01.003.

Sun, B., Noguchi, T., Cai, G., Zhao, W., 2021. Effect of temperature and relative humidity on the development of the compressive strength of surface-layer cement mortar. Constr. Build. Mater. 281, 122626. https://doi.org/10.1016/j.conbuildmat.2021.122626.

Tran, V.Q., 2022. Machine learning approach for investigating chloride diffusion coefficient of concrete containing supplementary cementitious materials. Constr. Build. Mater. 328, 127103. https://doi.org/10.1016/j.conbuildmat.2022.127103.

Štrumbelj, E., Kononenko, I., 2010. An efficient explanation of individual classifications using game theory. J. Mach. Learn. Res. 11, 1–18.

Wang, X., Huang, F., Cheng, Y., 2016. Computational performance optimization of support vector machine based on support vectors. Neurocomputing 211, 66–71. https://doi.org/10.1016/j.neucom.2016.04.059.

Wickramarachchi, D.C., Robertson, B.L., Reale, M., Price, C.J., Brown, J., 2016. HHCART: an oblique decision tree. Comput. Stat. Data Anal. 96, 12–23. https://doi.org/10.1016/j.csda.2015.11.006.

Xu, Y., Yuan, Q., Dai, X., Xiang, G., 2022. Improving the freeze-thaw resistance of mortar by a combined use of superabsorbent polymer and air entraining agent. J. Build. Eng. 52, 104471. https://doi.org/10.1016/j.jobe.2022.104471.

Yao, C., Shen, A., Yin, L., Dai, X., Wu, J., Guo, Y., 2024. A strength-based mix design method of fly ash concrete with superabsorbent polymer based on Powers' model. Constr. Build. Mater. 417, 135295. https://doi.org/10.1016/j.conbuildmat.2024.135295.

Yi, S.-T., Yang, E.-I., Choi, J.-C., 2006. Effect of specimen sizes, specimen shapes, and placement directions on compressive strength of concrete. Nucl. Eng. Des. 236 (2), 115–127. https://doi.org/10.1016/j.nucengdes.2005.08.004.

Zhang, J., Ding, C., 2025. Simple yet effective adaptive activation functions for physics-informed neural networks. Comput. Phys. Commun. 307, 109428. https://doi.org/10.1016/j.cpc.2024.109428.

Zhang, L., Jánošík, D., 2024. Enhanced short-term load forecasting with hybrid machine learning models: catboost and XGBoost approaches. Expert Syst. Appl. 241, 122686. https://doi.org/10.1016/j.eswa.2023.122686.

Zhao, S., Guan, X., Qiao, G., Lyu, J., 2022. Predicting relative compressive strength of concrete containing superabsorbent polymers. Cem. Concr. Compos. 133, 104689. https://doi.org/10.1016/j.cemconcomp.2022.104689.

Zheng, Q., Kulasekera, K.B., Gallagher, C., 2010. Local adaptive smoothing in kernel regression estimation. Stat. Probab. Lett. 80 (7–8), 540–547. https://doi.org/10.1016/j.spl.2009.12.008.

Zhong, P., Wyrzykowski, M., Toropovs, N., Li, L., Liu, J., Lura, P., 2019. Internal curing with superabsorbent polymers of different chemical structures. Cement Concr. Res. 123, 105789. https://doi.org/10.1016/j.cemconres.2019.105789.